Contents lists available at ScienceDirect

Coastal Engineering

journal homepage: www.elsevier.com/locate/coastaleng

Ripple and sandbar dynamics under mid-reflecting conditions with a porous vertical breakwater

M. Cobos[a,*], L. Chiapponi[b], S. Longo[b], A. Baquerizo[a], M.A. Losada[a]

[a] Instituto Interuniversitario de Investigación del Sistema Tierra, Universidad de Granada, Avda. del Mediterráneo s/n, 18006 Granada, Spain
[b] Dipartimento di Ingegneria e Architettura (DIA), Università di Parma, Parco Area delle Scienze, 181/A, 43124 Parma, Italy

A B S T R A C T

This research is an experimental study of ripple and sandbar dynamics under regular and random waves in partially reflective conditions. As part of this study, a series of small-scale flume experiments were performed that reproduced the growth and migration of the bedforms, starting from a flat bed or rippled bed, with sediment transport in the bedload regime.

The results showed that the evolution and dynamics of sandbar geometry were slower processes than the evolution of ripples. Moreover, they were governed by the wave field, reflective conditions, and sediment characteristics. Sandbar generation was controlled by the intensity of reflection, whereas the location of the crests (or deposition and erosion areas) was constrained by the phase shift of the reflected waves. Significant differences were also found between sandbars under regular and random waves. Sandbars under regular waves showed flat or practically flat troughs. In contrast, sandbars under random waves were almost uniformly covered by ripples.

The experimental results showed that the concurrence of ripples and sandbars under partially reflected waves has a spatially modulating effect on ripple characteristics (i.e. growth, shape and migration celerity), which could not be consistently interpreted by using the classical formulas valid for ripples under progressive waves and/or without large-scale bedforms. This variability was more pronounced for regular waves than for random wave trains. Larger ripples develop in the nodes of the free surface envelope (more or less corresponding to the sandbars crests), whereas smaller ripples occurred in the antinodes (or sandbars troughs).

The statistics of ripples geometry and celerity were computed with a sample stratification, based on their position in reference to the sandbars. In addition, they were compared in two energetically equivalent tests with regular and random waves, respectively. Although ripples under random waves had a larger wavelength and height than ripples under regular waves, the celerity of migration was comparable. Our results showed that the sandbars modified the equilibrium geometry of ripples. Furthermore, because of roughness, streaming was induced by the highest and longest ripples in the sandbar crests.

The spatial modulation of the ripple celerity was found to be related to the local Lagrangian mass transport velocity, which was produced by the quasi-standing wave inside the bottom boundary layer at the grain-diameter scale.

1. Introduction

Surface waves and currents in shallow water interact with the bottom and induce bedforms of various shapes and characteristics. This occurs both in the laboratory as well as in natural settings. Knowledge of bottom processes in the presence or absence of these natural structures is fundamental for the quantification of sediment transport rate and for the computation of wave energy dissipation. Of these bedforms, ripples and sandbars occur in the nearshore region,

which is roughly limited offshore by the bar where incoming waves generally break. Such bedforms can be classified as follows: (i) ripples of wavelength $\lambda \approx O(10^{-1})$ m (roughly the fluid particle semi-excursion near the bottom); (ii) dunes and antidunes of wavelength $\lambda \approx O(10^{0})$ m; (iii) bars of wavelength $\lambda \approx O(10)$ m; and (iv) sandbars of wavelength $\lambda \approx O(10^{2})$ m (the approximate wavelength of the free surface waves).

The fluid-particle interaction processes that generate these geomorphological structures have been widely studied, as reflected in the variety of the theoretical approaches, laboratory experiments, and field

measurements. Early research on ripple marks under oscillatory flow was performed by Hunt [1], followed by Darwin [2] and Ayrton [3]. The pioneering work of Bagnold [4,5] focused on the processes governing ripple generation, based on experimental results obtained in an oscillating wave tank. He detected a critical velocity of the fluid near the bottom, at which the grains start to move. Under stationary conditions, when sediment is in motion but not lifted, a stable pattern of bedforms develops, with steepness (height to length ratio) <0.10. These are known as "rolling-grain ripples". Such ripples are stable for speeds up to twice the previously mentioned velocity. As steepness increases, a vortex develops, which moves the sediments up to the crest and eventually traps the smallest grains. This modifies the scenario and creates a new type of bedform called "vortex-ripples", which spread out quickly and eliminate the rolling-grain ripples (Sleath [6]).

The sediment motion threshold has been studied by various authors, such as Bagnold [4] and Komar and Miller [7] (see Losada and Desiré [8] for a comprehensive list). Komar and Miller [7] specified two thresholds: (i) a sediment motion threshold for a laminar boundary layer (applicable to very small grains with $d < 0.05$ cm); (ii) a sediment motion threshold for a turbulent boundary layer (applicable to larger grains). In both cases the threshold depends on the maximum fluid velocity and the orbital diameter near the bottom. Losada and Desiré [8] and Losada et al. [9] proposed a general equation for incipient sediment motion by including the Reynolds number and extending the analysis to turbulent regime.

Wiberg and Harris [10] related the orbital velocity amplitude and the mean sediment grain size to the ripple type. The ripples observed were thus classified in three types: (1) orbital ripples (wavelength proportional to near-bed wave orbital diameter, $2A$), with $2A/d_{50} < 2000$; (2) anorbital ripples (wavelength practically independent of the near-bed wave orbital diameter), for values $2A/d_{50} > 5000$; (3) sub-orbital (with the possibility of both orbital and anorbital scalings), with $2000 < 2A/d_{50} < 5000$.

Most theoretical studies on geomorphological evolution assume that a horizontal bed of non-cohesive fine sands perturbed by a monochromatic flow motion is in the generalized motion state, and sediment transport modifies the bed sediments according to the Exner equation. The first of these studies was performed by Kennedy [11], whose description of the evolution of bedform amplitude assumed a potential flow in shallow water. He characterized the bottom patterns on the basis of the Froude number as well as on the local shift between sediment transport and fluid velocity. Although this local shift is known to play a key role, most models of bed evolution do not include its effect. Near the bottom, a boundary layer (BBL) develops, limited by the interface with the sediments bed, where the no-slip condition is applied, and by the external region. The BBL has certain particularities stemming from the flux regime and bed roughness. Generally speaking, the irrotationality of the flow field is not applicable. This question was addressed by Vittori and Blondeaux [12], who developed a perturbation model based on the stream function as influenced by the wave-driven currents. Their research related the grain Froude number to the Reynolds BBL number and the nature of ripples. However, they dealt with weak non-linear effects, which in real contexts are relevant. Certain hypotheses of the model are usually not satisfied. These include the assertion that sediment grain size is much smaller than the thickness of the viscous boundary layer, and that ripple amplitude is smaller than viscous BBL thickness. This signifies that non-linear terms become progressively more important in the vorticity equation.

There is a large body of literature that focuses on the experimental analysis of bedforms because of the complexity of the analytical approach. Some of those studies found semi-empirical relations between bed features, sediment flux in various conditions, and the geometric shape of the bottom in stationary conditions. Laboratory flume experiments were performed in which the bottom was allowed to evolve until a stationary state was reached. The resulting equilibrium bedforms were then measured and analyzed.

Nielsen [13] analyzed data obtained in various experiments with regular and random waves (Manohar [14], Mogridge and Kamphuis [15], Dingler and Inman [16], Nielsen [17], Allen [18]). He formulated an equation for ripple wavelength and height in the laboratory, depending on the Shields parameter, with empirical coefficients. After analyzing the experimental data in Inman [19] and Dingler [20], he extended the analysis to field ripples and formulated a similar equation for predicting ripples in the field and under turbulent oscillatory boundary layers (Nielsen [21]).

Other studies analyzed bedform shape, forced by different wave types. For this purpose, the researchers measured the migration velocity, transition stages, and relict shape of the bedforms. Faraci and Foti [22] performed a comprehensive experimental analysis of the evolution of ripple characteristics under progressive regular and random waves on a horizontal bed. They observed a ripple migration velocity of up to ≈40 cm h^{-1}. Smith and Sleath [23] carried out a spectral analysis of the bottom profile with a view to studying the response time of the ripple-covered bed to a step change in the flux conditions (mainly a variation of the near-bottom amplitude of oscillation). Two growth mechanisms were observed for the new bed profile: in the first case, the new profile arose from a previously existing perturbation of the bed at the same wavenumber as that of the final bed; in the second case, the ripple wavelength gradually changed to adjust to the new conditions. In certain conditions both mechanisms were active. Doucette and O'Donoghue [24] performed laboratory experiments to analyze the influence of wave randomness on the temporal evolution of ripples.

Bed slope effects are considered quite relevant since ripples in a natural environment almost invariably occur on a sloping bed (Chang et al. [25]). The bed inclination affects the sediment transport rate and modifies the dynamics of the ripples (see, e.g., Damgaard et al. [26] and Messaros and Bruno [27]). For this reason, the experiments in our study include tests with a sloping bed, which shall be discussed in a forthcoming paper.

All these studies refer to bedforms outside of the breaking zone (so as to avoid the huge sediment transport effect associated with breakers), and where reflection is not important.

Field analyses and large-scale experiments are extremely rare (see Doucette and O'Donoghue [28] for a review). Nonetheless, Traykovski et al. [29] and Traykovski [30] obtained field measurements with a rotational sonar and used these data to analyze bed evolution in the spectral domain. Messaros and Bruno [27] carried out experiments in a large wave tank and found that ripple characteristics in presence of irregular waves in the laboratory are similar to ripples characteristics in the field. They also found a statistically insignificant difference between ripple steepness on a horizontal surface and on a sloped surface.

An important factor that must be included in the evaluation of experimental results is that the bed formation process and evolution under oscillatory flow is the long-term balance of offshore and onshore sediment transport. Although both terms can have relatively high values, the difference between them is usually quite small. This means that it takes a very long time to reach the equilibrium condition, or for ripples and other bedforms to be in balance with the forcing wave field. Furthermore, small variations in the forcing wave field can change the sign of the net sediment transport, and may eventually modify the sign of the velocity migration or the tendency of ripple height and wavelength to grow or to decay. The consequences of a very long time scale of bedform evolution and of the high sensitivity of the system are the following: (i) bedforms in the field cannot be in equilibrium with the forcing wave (plus currents) field since this varies notoriously; (ii) bed load transport rates in both the field and laboratory fluctuate even if hydraulic conditions are steady. This can be attributed to several factors, including the migration of bedforms (Turowski [31]). As a result, in regard to bedforms, steady state is more a conceptual description without any clear experimental evidence.

All of these experiments and models depict an accurate scenario of bedform characteristics in a set of real conditions. However, in the

vicinity of dikes, cliffs and steep sloping beaches, where waves do not break and simply reflect, a rhythmic bed pattern develops strongly linked to the reflection process (see Xie [32] and Irie and Nadaoka [33]). At best of our knowledge, to date this has not been studied with adequate in−depth analysis. An important role in bedform evolution is played by the Lagrangian velocity. By assuming potential theory and horizontal bed, Carter et al. [34] determined the theoretical reflection conditions needed to revert the mass transport and analyzed the general implications of mass transport near the bottom during the bedform generation process. Nevertheless, certain questions still require a more complete answer, such as how the bed evolves under partially reflective conditions and how the geometric features of the bedforms are influenced by the parameters that govern the reflection (Baquerizo and Losada [35]).

Landry [36] depicted ripple dynamics in the presence of a fully and partially reflecting breakwater. He considered the effects of vegetation on sandbar formation with a large set of experiments which led to the identification of certain key elements governing both the generation and dynamics of bedforms under a partially standing wave for the two cases of dominant bed load and suspended load. However, Landry's experiments were limited to high reflective ($R \approx 0.9$) and low reflective ($R \approx 0.2$) structures. In contrast, the analysis of the mid-reflective structures (a very common type of maritime structure) is missing. In addition, Laundry's research only considered the reflection coefficient to be relevant, and ignored the phase shift.

The research study presented in this paper experimentally analyzed the bedform generation and evolution processes, which were observed on a horizontal bed under a wave field with mid-reflective conditions. Regular and random non-breaking wave trains propagated and partially reflected at a vertical porous breakwater on non-cohesive fine sands to generate bedforms. The dominant sediment transport was in the bedload regime.

The paper is organized as follows. Section 2 describes the experimental setup used to study the spatial wave oscillations, characteristics of the reflection process, near-bed current and the geometric evolution of the bedforms. Section 3 analyzes the flux conditions, bottom morphology, as well as the growth and migration rate of the ripples. It describes how they are affected by the wave type and reflective conditions. After a discussion of key aspects in Section 4, Section 5 presents the conclusions derived from this research. Details of the LDV measurements and statistics of the ripples are given in the Appendices.

2. Experimental setup and procedure

2.1. Test facility

The laboratory experiments were carried out in the combined wave-current flume of the Andalusian Institute of Earth System Research (IISTA, University of Granada, Spain). The wave flume is 2300 cm long, 65 cm wide and 100 cm deep (Fig. 1), with glass walls. It is equipped at one end with a piston-type wave-maker, capable of generating regular and random waves and with an active wave absorption system (AWACS). As part of our experimental setup, there was a dissipative parabolic beach at the other end of the channel. A mobile sediments bed, 20 cm-deep, was placed at 1050 cm from the mid-position of the wave paddle. The still water depth was 40 cm except in reference to the sediment bed, where it was 20 cm (as measured from the still bed level). Two wooden ramps with a 1:2 slope made the transition between the fixed bottom and the sediment bottom.

The sediments were well-sorted with $d_{50} = 0.32$ mm, a geometric standard deviation $\sigma_g \equiv (d_{84}/d_{16})^{1/2} = 1.59$, a relative density $s \equiv \rho_s/\rho = 2.65$, and an angle of repose of $31°$. A porous breakwater with vertical walls, made of pebbles and with a mean size of 4 cm, was placed 250 cm from the initial section of the sediment bed, buried in the sand at a depth of 5 cm.

The free surface elevation was measured with eight acoustic level sensors (UltraLab® USL 80D by General Acoustics, sensor model USS635) (A to N in Fig. 1a) placed above the flume, with an overall accuracy of 0.05 cm and a sample frequency of 20 Hz. For certain tests, the data from sensor D were found to be corrupted and could not be used.

Velocity measurements were taken with a TSI 2D laser Doppler velocimeter (LDV), which recorded vertical and horizontal flow velocities. The measurement volumes were located in the vertical sections in the mid-plane of the flume, and corresponded to the crests and troughs of the sandbars (#1 to #6 in Fig. 1b). The vertical distance between the measurement volumes was 1 cm. To improve the signal to noise ratio (S/N), tracers were added to the fluid. This made it possible to achieve a data rate with a minimum value equal to ≈30 Hz (near the bed because of suspended sediments) and maximum values of up to ≈400 Hz. The uncertainty in LDV measurements was approximately 1% of the estimated velocity (see, e.g., Longo [37] with the same equipment in the same flume).

The geometry of the sediment bottom was recorded with two digital cameras (Sony Cyber-Shot DSC-P200, 2304×3072 pixels) installed on a tripod. Their position gave them a side view of the flume and a plane of the optics at 200 cm from the glass wall of the flume. The focus plane was located inside the flume near the internal wall. With this setup, the resolution was equal to 0.6 mm/pixel. To avoid disturbances due to light reflection, a black canvas was placed behind the cameras covering the test section. Every 20 min, the experiment stopped for a short time until the fluid and sediments were at rest. Then a snapshots of the bed profile was taken and the experiment continued. This was done 8-15 times in order to monitor bed evolution.

2.2. Experimental procedure

In the course of this research, ten tests were performed, six with regular waves and four with random waves, based on the parameters in Table 1. In most of the tests, the sediment bed was flattened before beginning the wave attack. Exceptions were Tests 008-010, which started with the sediment bed geometry from the previous test. Four more tests were carried out with a wave period of 1.7 s. In these experiments, the wavelength was nearly equal to the sediment bed length (l_b=2.5 m), and the harmonic generation caused by the step (see Losada et al. [38] or Ting et al. [39]) was an additional process in an already complex system. Since this process could have dominated the effects of the reflection, these experiments were not included in the analysis. The water temperature was stable (ranging from $18°$ C to $20°$ C), the wave-maker was periodically calibrated, and the location of the cameras was verified.

For the random wave tests (Test 007-010), a JONSWAP spectrum was chosen with standard parameter values but with the peak enhancement value equal to 50, and with a limited band of frequency, in order to generate more than 95% of the energy stored in waves with a length of less than 250 cm (the length of the sediment bed).

2.3. Image analysis of the bed

There are various techniques that can be used to record the geometry of the bed profile. Their respective accuracy levels are 1–10 mm for bedform heights ranging from 6 to ≈130 mm in laboratory conditions. These techniques are listed in Table 2. Our tests used a technique based on image analysis, as described in Baglio et al. [40] and Faraci and Foti [22]. Two digital cameras on the side of the flume take snapshots at certain times. The snapshots are processed as follows: (1) the blue chroma signal is converted to a grey scale, which most efficiently detects the sediment-water interface; (2) the contrast is modified in order to enhance the image; (3) the pixels of the image are grouped into two sets by means of a k-means algorithm [41], thus converting the image into a 1-bit image (black and white image); (4) a
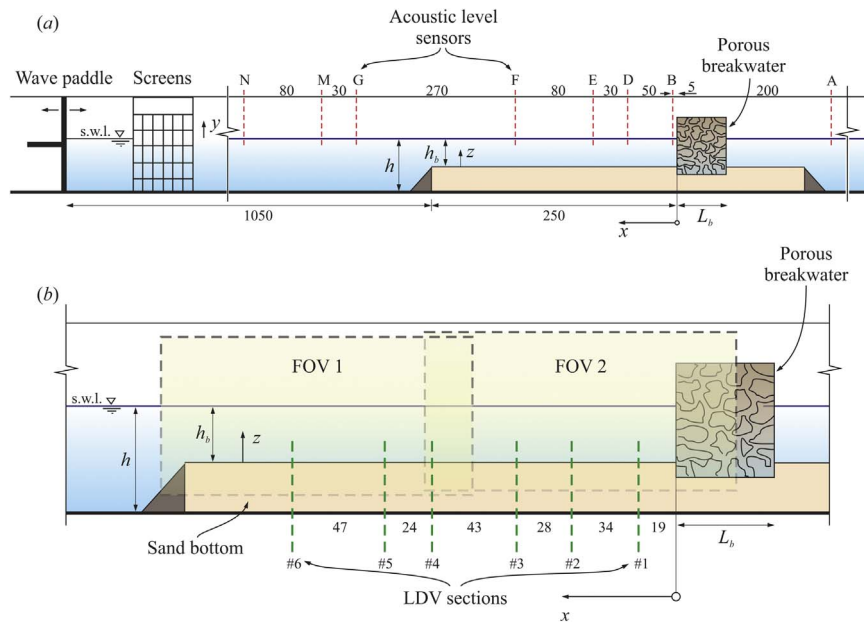
Fig. 1. Schematic description of the flume. (a) The section of measurements of the acoustic level sensors A-N; (b) the sections of LDV measurements #1–#6 and the Field of View (FOV 1 and FOV 2) of the two cameras. $h = 40$ cm is the still water depth; $h_b = 20$ cm is the still water depth where sediments are present; $L_b = 50$ cm is the porous breakwater width. The sizes are in centimeters.

Table 1
Parameters of the experiments. Case column: 'R' stands for regular waves; 'I' for random (irregular) waves; 'F' for flat bed; and 'P' for partial reflection. T and T_p are the period and the peak period for regular and random waves, respectively; H and H_{rms} are their wave height and the root mean square wave height; L is the corresponding wavelength; c is the phase celerity computed according to the theoretical dispersion relation; u_{bo} is the amplitude of the bottom velocity computed according to the potential flow theory, including the reflected component; A is the recorded wave orbital amplitude; $Ro = w_s/(\kappa u^*)$ is the Rouse number where w_s is the sediment settling velocity; and u^* is the friction velocity, $\kappa = 0.4$ is the von Kármán constant; $Re = u_{bo}A/\nu$ is the Reynolds number (ν is the kinematic viscosity of the fluid); and $Re_d = u_{bo}d_{50}/\nu$ is the sediment Reynolds number; $\psi = u_{bo}^2/((s-1)gd_{50})$ is the mobility number. In the first column, the symbol [a] indicates that no sediment motion was recorded; [b] indicates that LDV velocity measurements are available.

Test	Case	T, T_p (s)	H, H_{rms} (cm)	L (cm)	c (cm/s)	u_{bo} (cm/s)	A (cm)	Ro	Re ($\times10^3$)	Re_d	ψ	Duration (min)
001[a]	RFP	1.05	4	129	123	15.8	2.64	12	4.2	51	5	20
002[a]	RFP	1.05	5			19.8	3.31	10	6.6	63	8	20
003	RFP	1.05	6			23.8	3.98	10	9.5	76	11	160
004[a]	RFP	1.30	4	167	129	18.2	3.78	11	6.9	58	6	40
005	RFP	1.30	5			23.0	4.75	10	10.9	74	10	200
006[b]	RFP	1.30	6			28.2	5.83	9	16.5	90	15	200
007[b]	IFP	1.30	6			27.5	5.69	9	15.6	88	15	300
008	IFP	1.30	7			32.4	6.67	9	21.7	104	20	320
009	IFP	1.30	7.5			35.3	7.30	8	25.7	113	24	280
010	IFP	1.30	8			37.8	7.81	8	29.5	121	28	240

Table 2
Characteristics of measurement techniques used in the ripple tests available in the literature. RSS, SRP, and LDS are rotational side-scan sonar, sand ripple profiler and laser displacement sensor, respectively. η_r is the ripples height; the first and second values indicate the minimum and maximum ripples height, respectively.

Reference	Measurement technique	Test section length (cm)	Uncertainty (mm)	η_r (mm)
Faraci and Foti [22]	Camera devices	600	–	9.2–21.2
Smith and Sleath [23]	Mecasonic sonar	63	<3.15	4.46–43.25
Traykovsky [29,30]	RSS	700	<3.5	30–250
Doucette and O'Donoghue [24]	SRP and LDS	160	<10	13–128
Messaros and Bruno [27]	Sediment comb	100	<1	6–24
Landry [36]	Camera devices	2300	<2.117	6–20
Present study	Camera devices	250	<2.5	5–20

Gabor filter is used to emphasize the contours; (5) a tracking algorithm is applied to locate the bed profile on the pixel scale; (6) after calibration, the pixel position is converted into a geometric length scale.

The cameras in this setup provided a satisfactory resolution of the images (≈0.6 mm/pixel) in compared to the size of the measured ripples and sandbars (Landry [36]). The uncertainty in the tracking algorithm was approximatively equal to 2.5 mm, and the maximum relative error was less than 10%. Fig. 2 shows a typical profile recorded with camera 2 for one of the tests. Three of the eight acoustic sensors are visible at the top of the photo.

Some disturbances appeared in the bed profile at the offshore boundary of the beach because of the scour produced at the toe transition. For this reason, the first 10 cm were not considered in the analysis. The geometric characteristics of the bedforms were extracted with a zero up-crossing analysis after removing the noise with a low-pass filter. In this way, the 95th percentile of the elevation distribution (Traykovski [30]) was saved and the residual 2% was rejected. Then ripples and sandbars were separated by filtering them again with a cutoff wavenumber equal to $\lambda^{-1} = 0.05 \, \text{cm}^{-1}$ (detected by means of visual inspection, see Landry [36]).

A major variable involved in ripples and bedforms dynamics is the celerity of migration, often attributed to wave skewness and to wave asymmetry (Crawford and Hay [42], Traykovski et al. [29]). Bedforms are generally not fixed and vary according to the features of the flow field. In most cases, their shape, wavelength, and eventually the inclination of the sides (or position) all tend to vary. Migration celerity is usually detected by measuring the position of bedform crests at different times. The process is time consuming and hinders a thorough analysis of the data, in particular when there is a high data rate of images that are recorded in order to monitor the time evolution of the celerity, as happens in studies on bedforms and their adaptation to varying flow field conditions. This method is also subject to error since bedform crests are often rounded and difficult to detect.

An automatic detection algorithm (short-length cross-correlation, SLCC) was developed in our data analysis. A similar technique was adopted with acoustic measured bed profiles in Crawford and Hay [42] and in Hoekstra et al. [43]. This detection algorithm is based on the cross-correlation of the digitized bedform profiles after dividing the long-space signal into shorter segments. The result is a sliding window cross-correlogram, which is the counterpart in the space domain of the Short-time Fourier Transform. The bedform profiles recorded at times t_1 and t_2, with a time lag $\Delta t = t_2 - t_1$, are sampled with a window of a given width. After cross-correlating the same window for the two bed profiles, the peak of the cross-correlation function gives the average space-shift Δx of the bed profile. The average migration celerity of the bedforms within the sampling window is equal to $c_b = \Delta x/\Delta t$. The result is slightly sensitive to the width of the sampling window, which acts as a filter. If the window size is smaller than the length of the bedforms, the algorithm can fail.

In order to validate the algorithm, a single bed profile was studied. A manual detection of the ripple peaks was performed, and the ripple

celerity was computed as the ratio between the peak displacement and the interval time between the two snapshots (20 min). Fig. 3 shows the comparison of the manual and automatic detection algorithm celerity. The difference between the methods is almost negligible except where aliasing occurs or where the number of peaks is different in the two snapshots (e.g., at $x = 50$ cm a new ripple is created).

3. Results

The analysis and interpretation of the initial conditions and the results of the experiments are usually expressed by specifying relations between a set of variables, which represents the geometrical features of the bedforms, flux properties, bed characteristics, and the dominant transport process (see, e.g., Yalin and Russell [44], Sleath [45]):

$$(\lambda, \eta, c) = f(A, s, Re, Re_d, \psi, Ro, t), \tag{1}$$

where the orbital velocity amplitude or water semi-excursion $A = u_{b0}/\omega$ depends on the root mean square wave height H_{rms} and on the peak period T_p. Nonetheless, they also depend on wave transformation processes, characterized by parameters such as the beach slope $\tan\beta$ and the complex reflection coefficient given by its modulus K and phase Φ. In Expression (1), $s = \rho_s/\rho$ is the relative density of the sediments; $Re = u_{b0}A/\nu$ is the Reynolds number; $Re_d = u_{b0}d_{50}/\nu$ is the sediments Reynolds number; $\psi = (A\omega)^2((s-1)gd_{50})^{-1}$ is the mobility number; $Ro = w_s(\kappa u^*)^{-1}$ is the Rouse parameter; and t is a time scale. In the field it has been inferred that wave nonlinearity results in asymmetric velocity distribution (typically larger onshore velocity for shorter periods and weaker offshore velocity for longer periods) which, in turn, unbalances the sediment transport and forces ripples migration [29,46,42]. Hence the forcing terms of ripples migration are also related to the wave statistics.

There are other variables that may be indirectly or occasionally involved, such as the maximum near-bottom velocity u_{b0}. The wavelength λ and height η of the bedforms are scaled by the water semi-excursion length A (see Wiberg and Harris [10], O'Donoghue [47], Traykovski [30], among others). The migration velocity is scaled with the near-bottom velocity. The Shields parameter is defined as $\theta = 1/2f_w\psi$ (see Nielsen [17]), where f_w is the wave friction factor relating the maximum shear stress to the fluid velocity at the bottom (which are not simultaneous, see Jonsson [48]). The friction factor is computed as

$$f_w = \exp\left(5.213\left(\frac{2.5d_{50}}{A}\right)^{0.194} - 5.977\right). \tag{2}$$

3.1. Description and analysis of the wave oscillations and its derived processes

The wave generated by the paddle propagates along the flume in deep water ($h = 40$ cm) and over the sediment bed ($h_b = 20$ cm) to reach the porous breakwater. Then the wave is partially reflected, partially transmitted past the breakwater, and partially dissipated
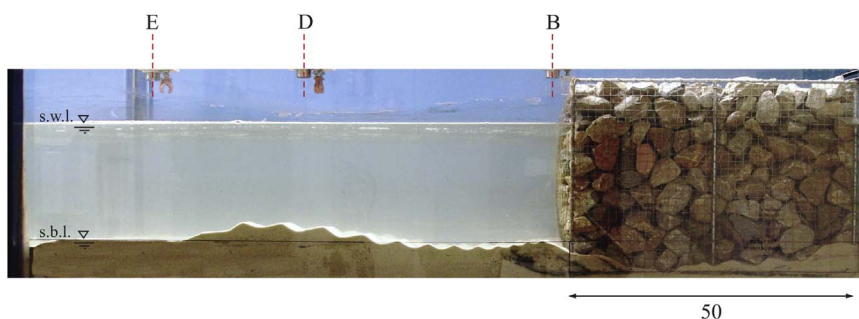

Fig. 2. FOV 2 snapshot of Test 006 after 60 min of wave action, where ripples and bed features can be observed.
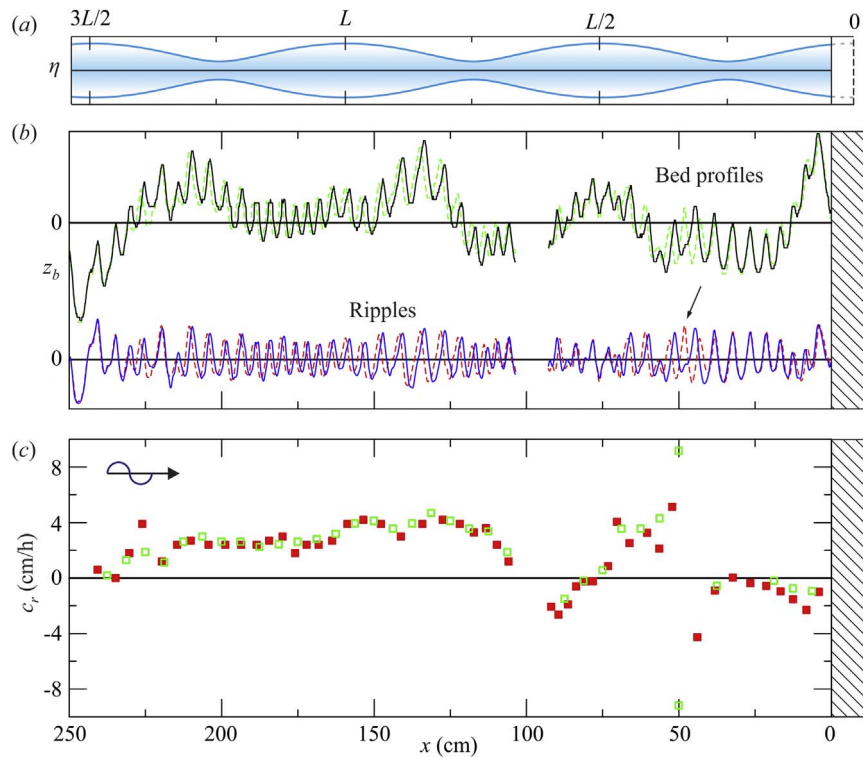
Fig. 3. Irregular waves. Comparison of ripple celerity estimated with the cross-correlation method and with the manual detection of peaks. (a) free surface envelope; (b) asymptotic bed profiles and ripples for Test 007, in reference to the last couple of frames (t=280 min, dashed lines, and t=300 min, continuous lines). The arrow indicates the development of a new ripple between the first and the second frame; (c) ripple celerity calculated with the cross-correlation method (window width equal to 125 mm or ≈$2\lambda_r$, empty symbols) and computed manually by detecting the crest-to-crest distance (filled symbols). Data are missing at $x \approx 95 - 100$ cm because of the presence of a vertical strut of the channel frame.

(Losada et al. [49] and Baquerizo and Losada [50]). The height-to-depth ratio and the steepness of the waves are similar to the steepness used for tests in other researches, with $H/h \approx 0.25$ and $H/L \approx 0.03$. Fig. 4a shows the free surface elevation for regular waves, and Fig. 4b for random waves, as recorded by sensors N to A (see Fig. 1 for the layout of the sensors). For regular waves, the free surface elevation was sinusoidal in the deeper part of the channel (where the depth $=h$). There was a negligible deviation from linear theory when the wave entered the sediment bed area (with water depth equal to $h_b < h$). A small residual wave was transmitted through the porous breakwater (sensor A). For irregular waves the effect of the water depth reduction was similar but less evident in the free surface elevation profile because of the multiple waves propagating with different celerities. Valuable information can be gained from the evolution of other more evident waves in the packets, such as the wave marked with a dashed line in Fig. 4 (sensors G-B). In all tests, for both regular and random waves, there was a significant reduction in amplitude at the quasi-nodes (see sensor D in Fig. 4), and a significant increment in the quasi-antinodes (see sensor E in Fig. 4). Both skewness and asymmetry can be observed which are addressed as responsible for ripples migration (see Crawford and Hay [42], and Traykovski et al. [29]). Fig. 5 shows a synthesis of the wave envelopes for all the tests. For irregular waves, the mean value of the highest 1/3 crests and troughs are shown. The important role of a non uniform wave envelope (and thus of the bottom shear stress and of bed load transport) was documented by Yu and Mei [51] in their analysis of sandbars under surface waves.

The theoretical location of the quasi-nodes and antinodes can be computed by using a reflection analysis. However, the location is only approximate because of the numerous wavelength components contributing to the wave field. The modulus and the phase shift of the reflection were computed with the method proposed by Baquerizo [52] and Baquerizo et al. [53] (see Appendix A). Table 3 shows the results obtained from sensors N-M-F at water depth h, and from sensors E-D-B at water depth h_b, respectively. For random waves, the reflection

coefficients were assigned to the peak period wave. As expected, the porous breakwater modified the phase of the reflected wave, moving the first quasi-node onshore into the breakwater (negative phase shift) (Losada et al. [38] and Losada et al. [49]). A reflection phase shift is documented in literature for sloping breakwaters (Hughes and Fowler [54], Sutherland and O'Donoghue [55], Sumer and Fredsøe [56]).

As for the hydrodynamic field, the absence of wavebreaking reduced the wave set-up or set-down and the undertow was negligible. However, wave set-up on the lee side of the breakwater was non-negligible and forced a net flux directed offshore near the bottom through the breakwater (see Losada et al. [49]).

3.2. Bedform morphology

Following the classification in Wiberg and Harris [10] ($2A/d_{50} < 2000$) 2D orbital ripples were found in our tests. An in-depth analysis of the data made it possible to obtain the morphology of the ripples and sandbars as well as the time scale of their evolution. The near bottom velocity caused a stress that overcame the critical stress by inducing the general motion (Losada and Desiré [8] and Losada et al. [9]) under the quasi-nodes. Ripples started to develop inside the Bed Active Region (BAR). At the same time, though somewhat more slowly, sandbars began to emerge because of the mass transport induced in the BBL. Flat regions appeared between BARs as commonly observed in front of full reflective walls under the attack of regular waves (Gislason et al. [57]). The tests with random waves showed a similar bed structure, but without the flat regions, with ripples also present at the quasi-antinodes.

3.2.1. Ripple height analysis

Ripple height is usually regarded as dependent on the mobility parameter and on the ratio A/d_{50}. A simpler expression only considers the mobility number with a function empirically described by Nielsen [17]
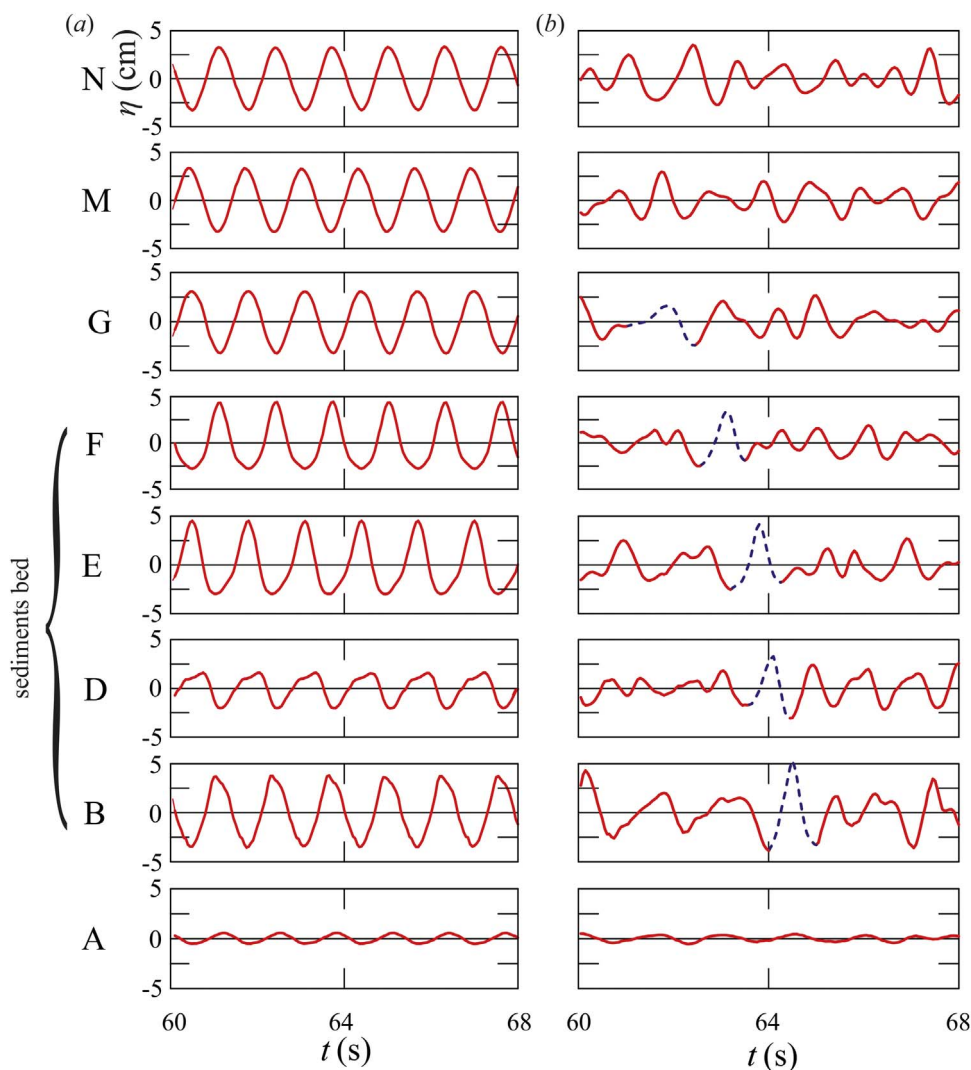
Fig. 4. Instantaneous free surface profiles for (a) Test 005 (regular waves), and for (b) Test 007 (random waves). The waves propagate from sensor N (the closest to the wave paddle) to sensor B (the closest to the porous breakwater). Sensor A is at the lee side of the breakwater and records the transmitted waves. The crest marked with a dashed line in the irregular wave tests corresponds to the same individual wave and shows its along-channel evolution over the region closest to the porous structure.

$$\frac{\eta_r}{A} = 0.275 - 0.022\sqrt{\psi} \quad \text{for } \psi < 156, \tag{3a}$$

$$\frac{\eta_r}{A} = 21\psi^{-1.85} \quad \text{for } \psi > 10, \tag{3b}$$

for the laboratory and field, respectively. For field ripples the variables ψ and A refer to the significant wave height.

In the present study the ripples at the node-antinode and stoss-lee sides were analyzed separately. The results are shown in Fig. 6a, along with experimental data obtained by Faraci and Foti [22] for purposes of comparison. The median height in the nodes, lee-side, was found to be in good agreement with the experimental fitting by Nielsen in the laboratory. Ripples in the antinode stoss-side had a minimum height, particularly for the regular waves, which tended to leave a flat bed in the antinodes and in the scouring areas. Fig. 6b shows the ripples height adimensionalized by the orbital velocity amplitude, which was sampled based on the position in reference to the sandbars. The highest ripples developed at the crest of the sandbars, with tiny differences between the lee side and stoss side and with values over 50% higher than the ripples in the trough for random waves. Again, variability was considerably more evident for the regular waves since the ripple height in the crest was more than twice the ripple height in the trough. These

were marked on the bottom in a clear succession of scouring and flat bed (both almost without ripples), and sandbars crest covered by well-formed ripples. Nielsen's formula slightly overpredicted the experimental data in the crest, with a better agreement for the random waves tests. There was an evident correlation, depending on the envelopes and depending on the sandbars, given that the sandbars crests were almost in the nodes with a modest phase shift.

Fig. 7 shows the frequency of the heights for two corresponding energy tests with regular and random waves. For regular waves (see Fig. 7a), the lowest ripple height dominate the trough and the highest ripples are above the crest. In the case of random waves (see Fig. 7b), the maximum height is below 0.25 and the height distribution is well distributed in both crests and troughs. Table 4 lists the median values of the ripples height for sandbar geometry.

3.2.2. Ripple wavelength analysis

The wavelength of the ripples is often assumed to be a constant multiple of the orbital amplitude A, equal to $\lambda_r/A = 1.33$ if $\psi < 20$ (e.g. Bagnold [4], and Carstens et al. [58]). For a generic value of the mobility number ψ, the wavelength of the ripples is assumed to be dependent on the mobility number according to the following empirical
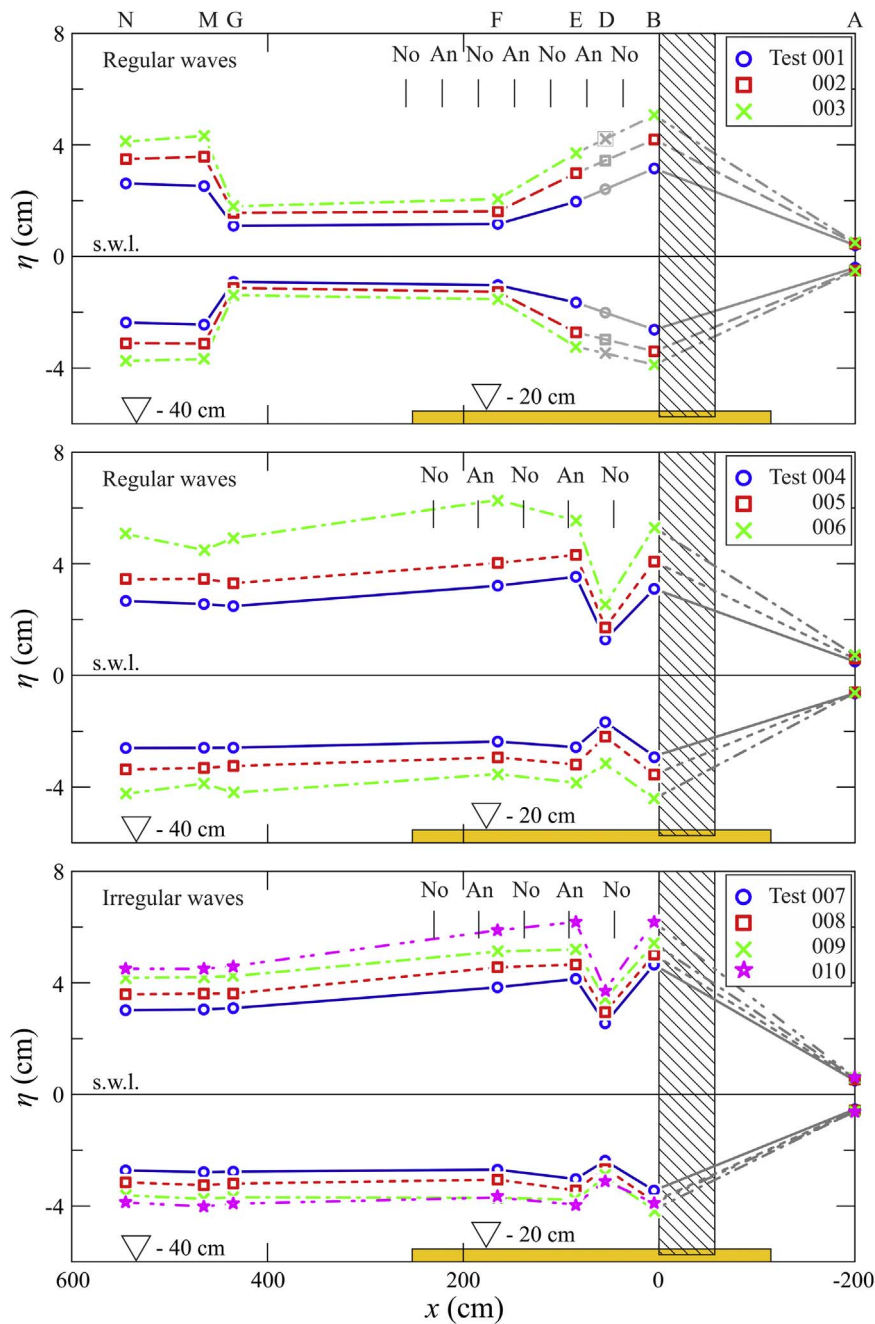
Fig. 5. Envelope of the free surface profile for all the experiments. The mean water level almost coincides with the still water level. 'An' stands for quasi-antinodal section and 'No' stands for quasi-nodal section. In Test 001, 002, and 003, data from sensor D at $x = 55$ cm are missing due to signal corruption. For random waves (Test 007-010), the envelopes of the trough amplitude $A_{t,1/3}$ and crest amplitude $A_{c,1/3}$ are shown, representing the average of the highest 1/3 values of troughs and of crests, respectively.

Table 3
Reflection coefficients computed according to Baquerizo [52]. $K = A_r/A_i$ is the ratio between the amplitude of the reflected and incident waves; and Φ is the angle of the shift between the incident and reflected waves. Subscripts 1 and 2 indicates the two groups of sensors G-M-N and D-E-F used to calculate the reflection coefficients. The missing data are due to the corrupted signal of sensor D. "R" and "I" following the test number stand for regular and irregular waves, respectively.

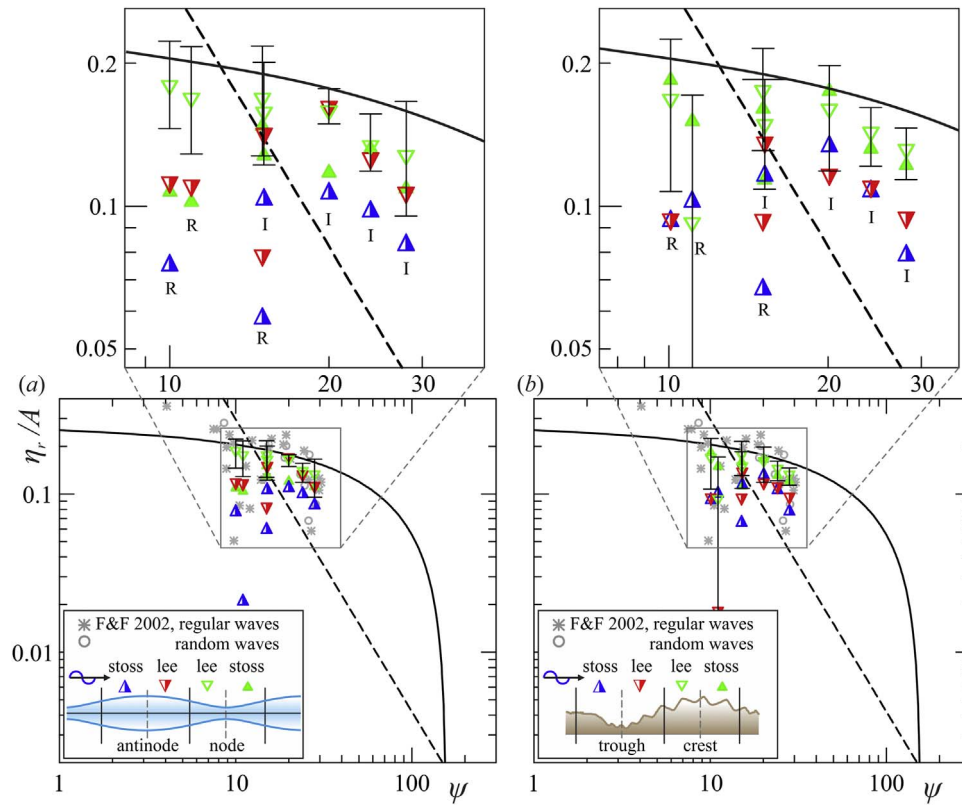| Test	001(R)	002(R)	003(R)	004(R)	005(R)	006(R)	007(I)	008(I)	009(I)	010(I)
K_1 (·)	0.499	0.502	0.504	0.530	0.544	0.503	0.507	0.488	0.476	0.469
Φ_1 (rad)	−1.017	−0.877	−0.835	−0.779	−0.825	−0.507	−1.081	−2.976	−0.951	−1.010
K_2 (·)	–	–	–	0.552	0.562	0.599	0.558	0.573	0.600	0.606
Φ_2 (rad)	–	–	–	−0.301	−0.318	−0.225	−0.527	−0.841	−0.321	−0.411

Fig. 6. Median ripple height sampled, based on their position with reference to (a) the free surface envelopes and (b) the sandbars. "R" and "I" stand for regular and irregular waves, respectively. The curves refer to the experimental fit by Nielsen [17] for the lab (bold line) and for the field (dashed line). The stars and circles are the results obtained by Faraci and Foti [22]. The error bars indicate the corresponding standard deviation.
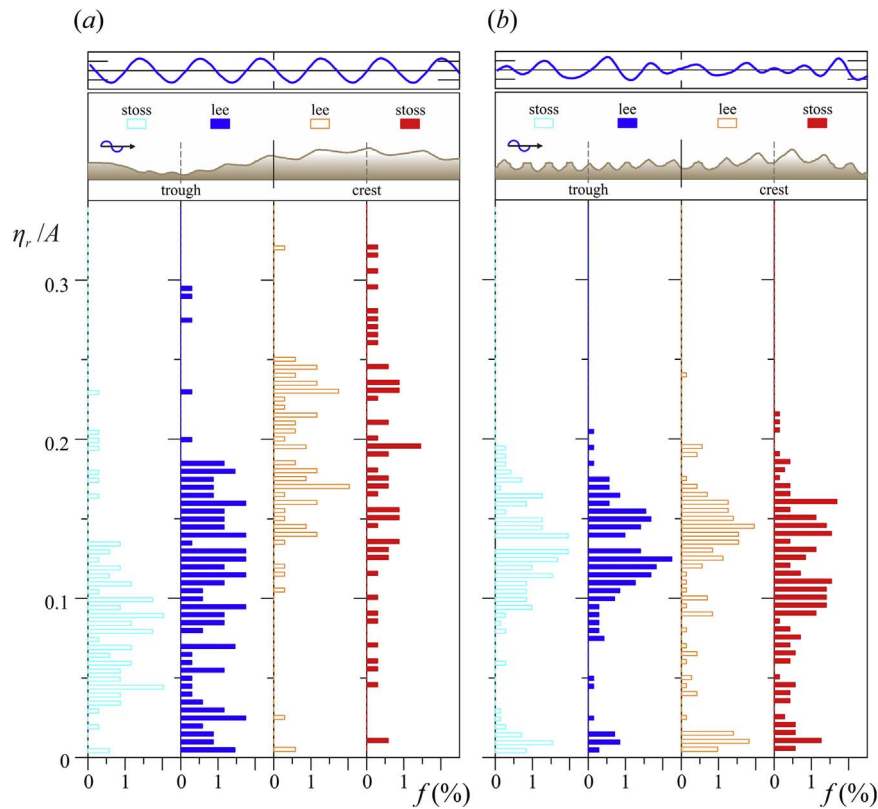

Fig. 7. Frequency of the ripple height based on their position with reference to the sandbars. (a) Test 006 (regular waves); (b) Test 007 (random waves).

equations formulated by Nielsen [17] for laboratory and field conditions, respectively

$$\frac{\lambda_r}{A} = 2.2 - 0.345\psi^{0.34} \quad \text{for } 2 < \psi < 230,$$

(4a)

$$\frac{\lambda_r}{A} = \exp\left(\frac{693 - 0.37\ln^8\psi}{1000 + 0.75\ln^7\psi}\right).$$

(4b)

Fig. 8a and b shows the experimental median wavelength of the ripples, depending on their position in reference to the surface envelopes and sandbars. The lee-side ripples are generally longer than the stoss-side ripples when the free surface envelope position is considered. In contrast, the ripples in the sandbar crests are about 20–40% longer than the ripples in the sandbar troughs. This is consistent with the experimental results obtained by Cataño-Lopera and García [59]. The comparison with Nielsen's formula for laboratory ripples shows a small

Table 4
Median ripple height, based on their position in reference to the sandbars. The data refer to the asymptotic regime, and values are non-dimensional with respect to the wave orbital radius *A*. "R" and "I" in the first column indicate regular and irregular waves, respectively.

Test	ψ	Crest		Trough		Crest	Trough	All
		Atoss	Lee	Stoss	Lee			
005(R)	10	0.184	0.167	0.095	0.093	0.172	0.095	0.114
003(R)	11	0.150	0.091	0.104	0.018	0.147	0.060	0.117
006(R)	15	0.159	0.174	0.068	0.092	0.171	0.077	0.117
007(I)	15	0.113	0.147	0.118	0.135	0.138	0.129	0.132
008(I)	20	0.168	0.159	0.136	0.115	0.164	0.120	0.139
009(I)	24	0.131	0.142	0.109	0.109	0.138	0.109	0.122
010(I)	28	0.121	0.130	0.080	0.093	0.129	0.087	0.097

overestimation of the formula, with a decreasing and monotonic median wavelength of the ripples for an increasing mobility number. The best agreement was found for the length of the ripple crests, whereas the trough ripples were much shorter than predicted. The numerical values are listed in Table B.1 in Appendix B for the ripples based on their position in reference to the sandbars. Fig. B.1 shows the wavelength statistics for two energetically equivalent tests with regular and random waves. Intriguingly, for regular wave conditions the range of the wavelengths is broader than for random waves, with a few long
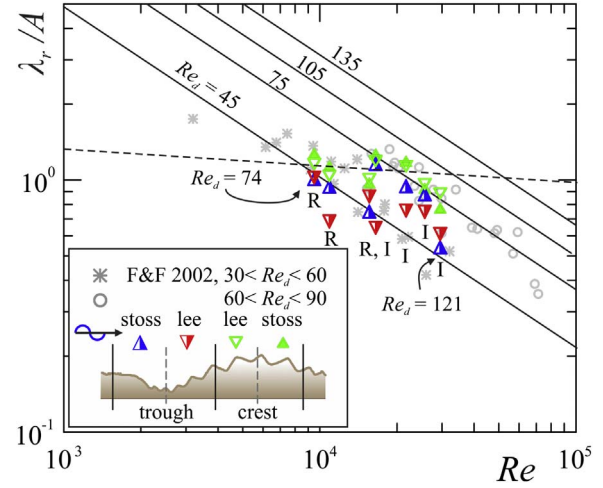

Fig. 9. Ripple wavelength as a function of *Re*. The triangles refer to our experiments, the stars and the circles refer to experiments with increasing Re_d by Faraci and Foti [22], the dashed line refers to Eq. (5), and the bold lines refer to Eq. (6) with $Re_d = 45, 75, 105, 135$. "R" and "I" stand for regular and irregular waves, respectively.
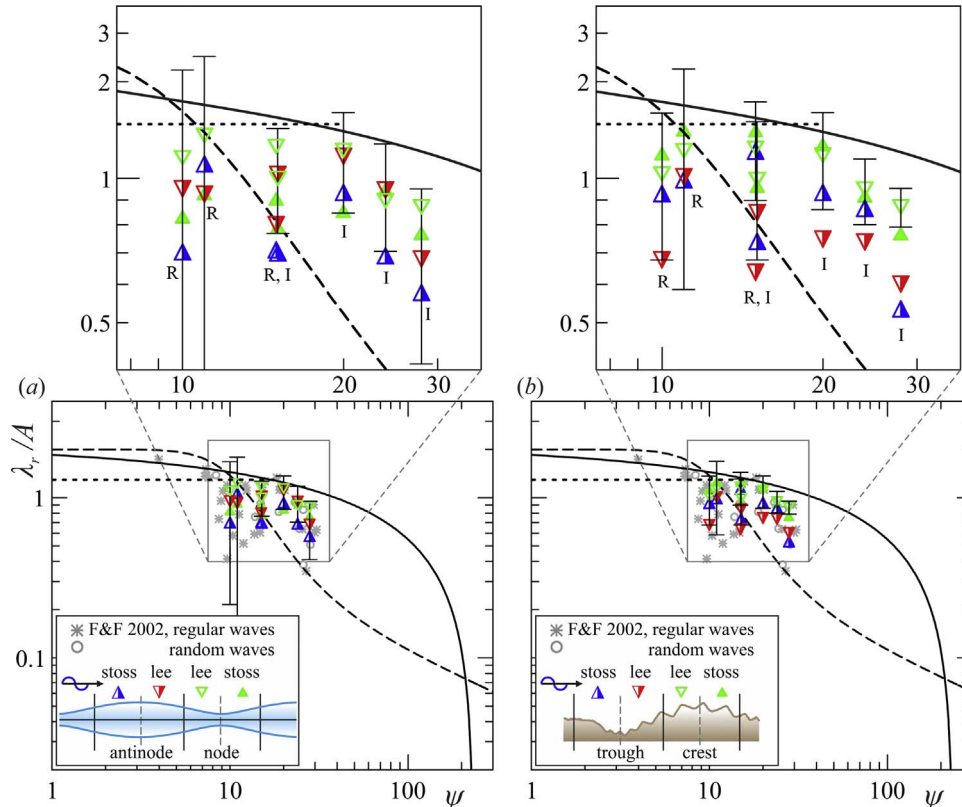

Fig. 8. Median ripple wavelength sampled based on their position with reference to (a) the free surface envelopes and (b) the sandbars. "R" and "I" stand for regular and irregular waves, respectively. The curves refer to the experimental fitting by Nielsen [17] for the lab (bold line) and for the field (dashed line); the dotted curve indicates the limit $\lambda_r/A = 1.3$ for $\psi < 20$. The stars and circles are the results obtained by Faraci and Foti [22]. The error bars indicate the standard deviation of the sub-samples.

ripples also in the troughs. There is no evident peak clustering. For random waves, the distribution is almost symmetrical with respect to a peak value, with a similar presence in the crest and trough. The wavelength and amplitude growth of the ripples in random waves conditions appears to be inhibited above and below a certain threshold, with most ripples within a restricted interval.

For low sediment transport rates, Sleath [60] discussed the numerous approximations and assumptions. He presented a theoretical evaluation of the limiting wavelength of vortex ripples as a function of the Reynolds number

$$\frac{\lambda_r}{A} = 2.04 Re^{-0.064}. \tag{5}$$

Later analyses highlighted the role of the Reynolds number of the sediments, Re_d. For ripples developed under progressive waves, Faraci and Foti [22] proposed the following two-parameter function

$$\frac{\lambda_r}{A} = 12 \frac{Re_d}{Re^{0.68}}. \tag{6}$$

Our experiments were performed in a bed-load regime (vortex ripples favors the suspended load regime) and the waves were not progressive but rather partially reflected at the porous breakwater. Consequently, there were certain differences when we compared wavelength in the experimental data as a function of Re with the results obtain by other authors (Fig. 9). Eqs. (5) and (6) both overestimate the wavelength of the ripples, particularly the ripples in the trough and the regular waves. The number of tests in the present study is not large enough to draw definitive conclusions regarding the structure of the two-parameter function. However, there is evidence that sandbars reduce the wavelength of the ripples for increasing Re, in particular for the ripples in the trough.

3.3. The steepness of the ripples

By interpolating experimental data, Nielsen [17] proposed a ripple steepness equal to Eq. (7) for laboratory and field conditions, respectively,

$$\frac{\eta_r}{\lambda_r} = 0.182 - 0.24\theta^{1.5}, \tag{7a}$$

$$\frac{\eta_r}{\lambda_r} = 0.342 - 0.34\theta^{1/4}. \tag{7b}$$

Fig. 10a and b show the experimental steepness of the ripples in our tests, with a stratified sampling based on their position in reference to the free surface envelope and to the sandbars, respectively. Table B.3 lists the numerical values of the median estimator. Ripples were found to be steeper in the quasi-node (crest) than in the quasi-antinode (trough), with a satisfactory agreement with Eq. (7a) for the quasi-node (crest) ripples. The decaying trend of the predicting formula for increasing ψ was not clearly perceived, but it was well within the variability of the samples represented by the vertical error bars. Fig. B.3 shows the statistics of the steepness for two tests with regular and random waves, respectively, which where energetically equivalent. The sample referred to the entire set of experiments, including the initial evolution starting in both tests from a flat bed.

A simple scheme for the evaluation of the maximum steepness of the ripples for a vanishing Shields parameter was presented in Nielsen [13]. When the ripples are regarded as a sequence of equilateral triangles with angles equal to the internal friction angle, the result is $(\eta_r/\lambda_r)_{max} = 0.5\tan\phi$. When a parabolic symmetric profile is assumed, the result is $(\eta_r/\lambda_r)_{max} = 0.25\tan\phi$. The experimental coefficient for $\theta < 0.2$ is between these two extreme models and is equal to 0.32. When the effects of a non zero local bed slope χ due to sandbars are also considered, this yields the following for a triangular shape
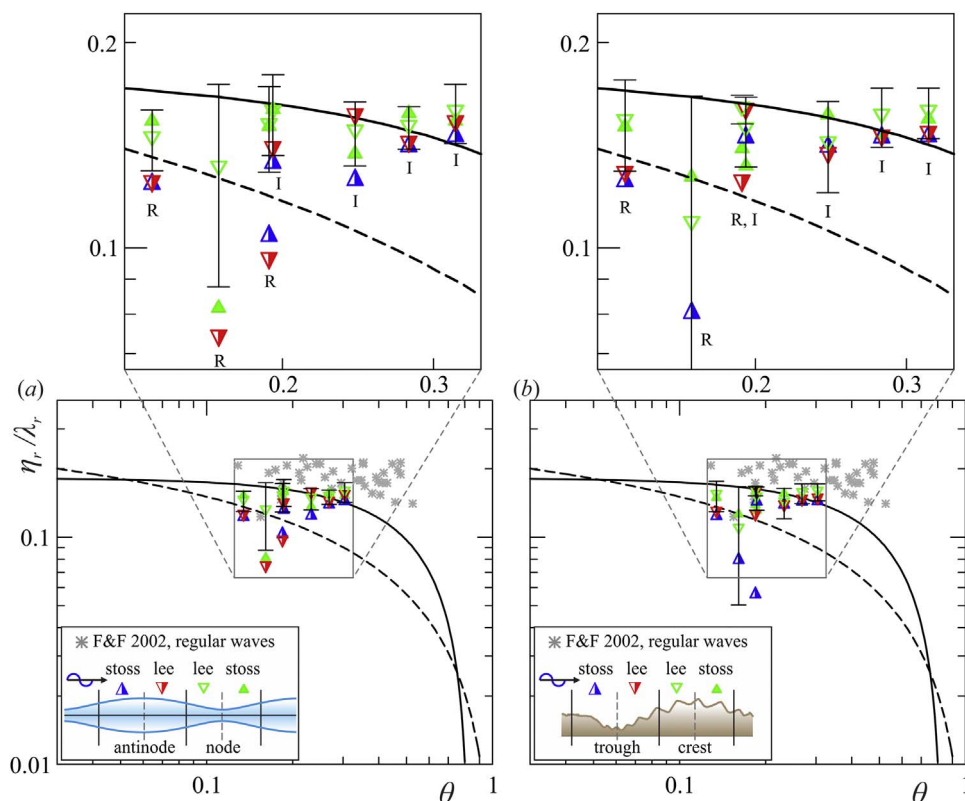

Fig. 10. Median ripple steepness sampled, based on their position in reference to (a) the free surface envelopes and (b) the sandbars. "R" and "I" stand for regular and irregular waves, respectively. The curves refer to the experimental fitting by Nielsen [17] for the lab (bold line) and for the field (dashed line). The stars are the results obtained by Faraci and Foti [22] for regular waves. The error bars indicate the standard deviation of the sub-samples.

$$(\eta_r/\lambda_r)_{max} = \frac{1}{\cot(\phi + \chi) + \cot(\phi - \chi)}, \tag{8}$$

which for $\chi \to 0$ reproduces the theoretical expression given by Nielsen for a flat bed. The overall effect of a non-zero local bed slope is the reduction of the maximum steepness of the ripples with respect to its value on a horizontal bottom, with the same reduced value for both an upward sloping as well as downward sloping bottom. In order to compare our data with the data in the literature, the experimental steepness of the ripples was corrected by dividing it by the coefficient

$$\Upsilon = \frac{2}{\cot(\phi + \chi) + \cot(\phi - \chi)}, \tag{9}$$

which yields $\Upsilon = \tan\phi$ for $\chi \to 0$ and $\Upsilon = 0$ for $\chi \to \pm \ \phi$.

Fig. 11 shows the distribution of the ripples steepness as a function of the Shield parameter θ, with the dashed line corresponding to $\eta_r/\lambda_r = 0.32\Upsilon$, for $\theta < 0.2$. The largest steepness variability was for the regular wave tests (Test 003-005-006), with a median steepness below the predictor.

Fig. 12 shows the behavior of ripples in the crests and troughs of the sandbars. The difference between the crests and troughs was minimal for random waves, but very evident for the regular waves.

3.3.1. Ripple migration celerity

Ripple migration velocity is crucially influenced by the spatial variation of the wave field as well as by added effects, which generate near-bottom currents or modulate the near-bottom fluid velocity. The presence of a partially reflecting porous breakwater is the primary cause of many of these effects. Since the reflection spatially modulates the wave field with quasi-nodes and quasi-antinodes, the wave set-up on the back of the breakwater induces a current that is directed offshore. The sandbars sequence thus spatially modulates the near-bottom boundary layer. In particular, the presence of the sandbars seems quite relevant since the characteristics of the ripples are better correlated with sandbars than with the free surface envelope. From this perspective, our analysis differs from Landry [36], who explicitly neglected sandbars in his study of superimposed ripples. We also mention the possible effects of wave skewness and of asymmetry, which in the field have been quoted as responsible for ripples migration (Traykovski et al. [29], Crawford and Hay [42]).

An overview of the processes involved in ripple celerity is shown in Fig. 13, in specific reference to Test 006 (regular waves) and in Fig. 14, in reference to Test 007 (random waves). The results show that for the regular wave test, ripple celerity is spatially modulated and slightly time varying, with a progressive adaptation to sandbar development

and slow migration. In the random wave test the ripple celerity still adapted to sandbar evolution. Nevertheless, time variations are quite limited near the breakwater and are more evident at the farthest sandbar. The maximum celerity has a phase shift with respect to the nodal section, which varies for the two wave attacks.

Fig. 15 shows the celerity statistics with the separation of the contributions in the crests and troughs, at the lee and stoss sides. The sample contains all the frames of the tests, including the frames during the initial growth of the ripples. Regarding the regular wave test, the main peak refers to zero celerity and a secondary peak refers to negative celerity (as opposed to the propagation direction of the incoming wave). In the random wave test, there are two frequency peaks, one corresponding to a positive celerity, and the other to a negative celerity. The positive celerity of the first peak slightly exceeds with respect to the negative celerity (in modulus) of the second peak. In the regular wave test, the ripples in the crest have the highest celerity, since the ripples in the trough were slowly migrating. In the random wave test, the difference in celerity between ripples in the crests and those in the troughs was less marked and the trough area was quite active. Fig. 16 compares the dimensionless median celerity of these experiments, separated in terms of ripples in the crests and ripples in the troughs as opposed to the mobility number. Data from other studies are shown in the same figure. The overall impression is that the process in our experiments was much less energetic than the process in the previous experiments. A comparison shows that our data reflects a
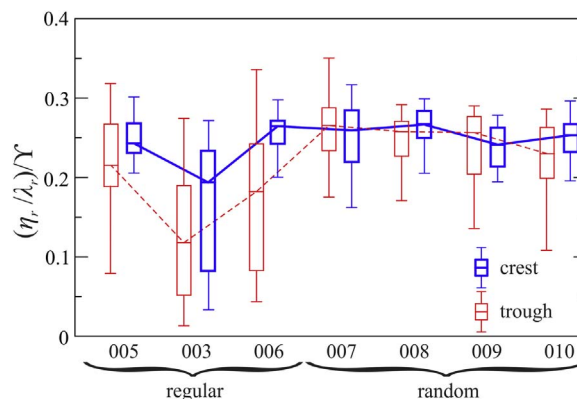
Fig. 12. Steepness of the ripples based on their position in the crests and troughs of the sandbars. The sequence of the tests corresponds to increasing mobility number, see Table 6.
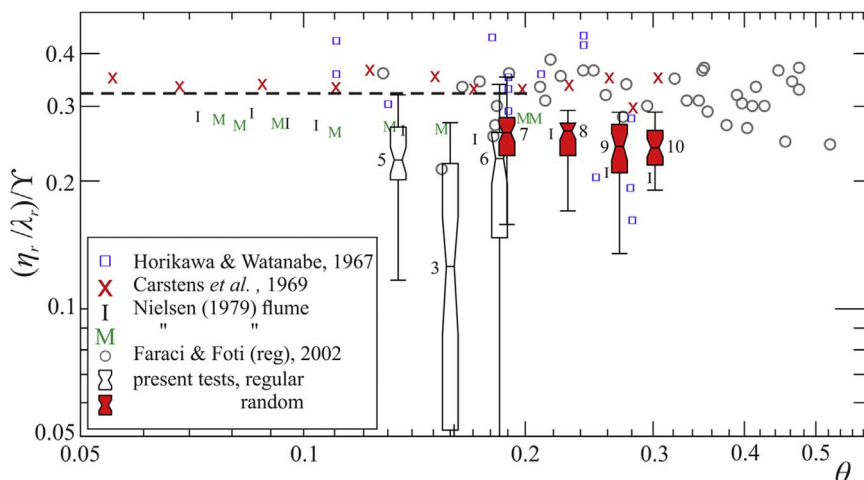
Fig. 11. Box and whiskers plot of the steepness of the ripples as a function of θ. Comparison to the data obtained by Horikawa and Watanabe [61], Carstens et al. [58], Nielsen [17], and Faraci and Foti [22] (only regular waves). Empty boxes refer to regular wave tests, and filled boxes refer to random waves. $\Upsilon = 2/[\cot(\phi + \chi) + \cot(\phi - \chi)]$ is a coefficient which includes the effect of the local bed slope χ due to the presence of sandbars.
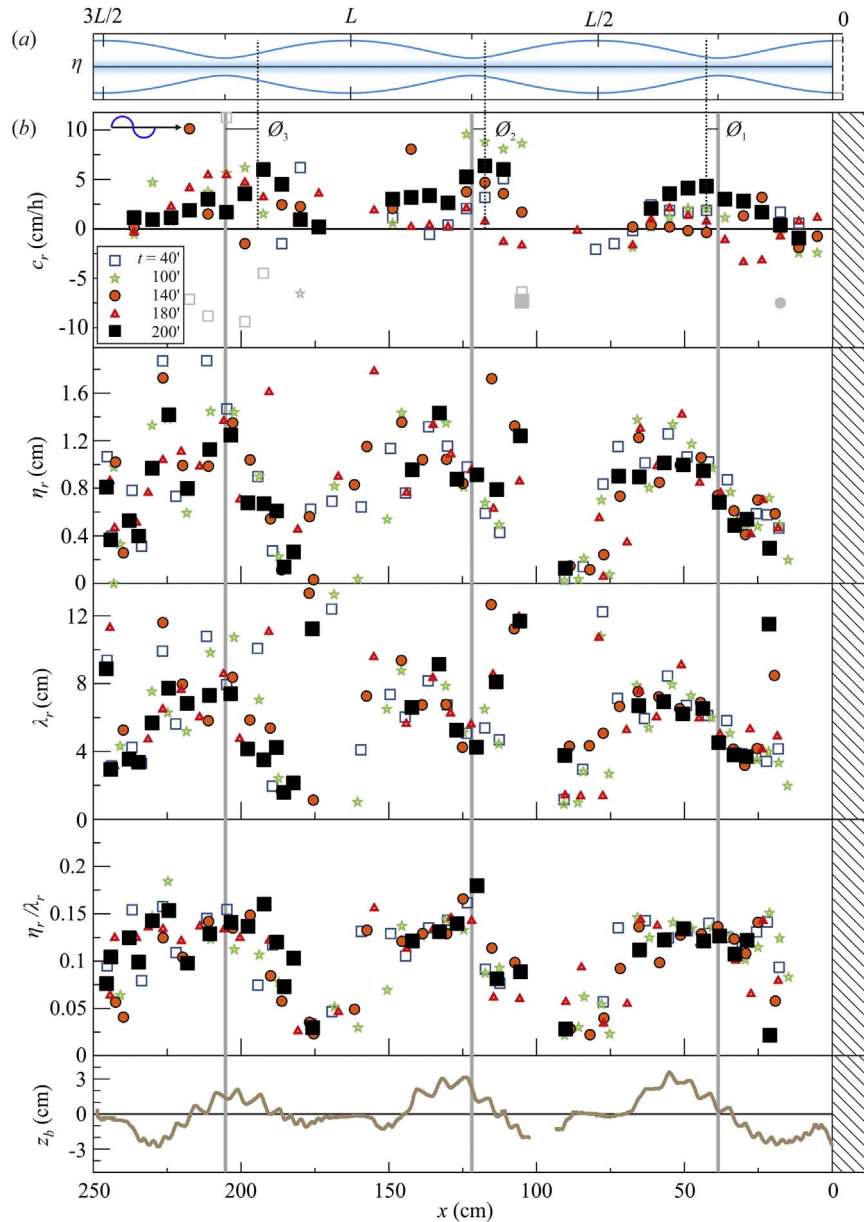
Fig. 13. Main characteristics of the ripples for Test 006 (regular waves). (a) Wave envelope; (b) celerity, height, wavelength, and steepness of the ripples at different times during the experiment. The last plot represents the bed profile at $t = 200$ min. Data are missing at $x \approx 95 - 100$ cm because of the presence of a vertical strut of the channel frame.

lower migration celerity.

Ripples respond to the local wave action by following the periodic onshore offshore oscillation, with a net movement dictated by the differences occurring during the cycle. This difference can also be due to a net fluid flow superimposed on the oscillation. Dingler and Inman [16] found a positive correlation between the migration celerity of ripples and a bottom wave-drift current, theoretically equal to $(5/4)u_{b0}^2 T/L$ for progressive waves. A generalization of the wave-drift current is the vertical profile of the near-bed Lagrangian mass-transport velocity u_L, which is related to ripple migration (Carter et al. [34], Gislason et al. [57] and Landry [36]). For partially standing wave with a phase shift of the reflected component, the Lagrangian velocity near the bottom is equal to

$$u_L = R\frac{\omega kA^2}{\sinh^2 kh}\sin(2kx + \Phi)\left(\frac{3}{2}e^{-2\xi} - \frac{3}{2} + 4e^{-\xi}\sin\xi\right)$$
$$+ (1 - R^2)\frac{\omega kA^2}{\sinh^2 kh}\left(\frac{3}{4}e^{-2\xi} + \frac{5}{4} - 2e^{-\xi}\cos\xi\right),$$

(10)

where $\xi = z/\delta$; and $\delta = \sqrt{2\nu/\omega}$ is the thickness of the boundary layer, with ν representing the eddy viscosity of the boundary layer (Carter et al. [34], Ng [62] and Landry [36]). In the case of standing or partially standing waves, it is worth highlighting that the horizontal Lagrangian velocity is subject to change sign in the vertical, provided that $R > 0.414$ [34]. Hence, a recirculation pattern of $L/4$-length causes bedload transport to move the sediments to the nodes and the suspension transport to move the sediments to the antinodes (Yu and Mei [51] and Landry [36]). This behavior has various consequences, since for graded sediments, the coarse particles (transported in bedload regime) have a net movement toward the nodes, whereas the fine particles (transported in suspension regime) have a net movement toward the quasi-antinodes, with a consequent particle segregation (Landry et al. [63]). However, this is a general scenario. In the experiments carried out in our study, sediment transport was in the bedload regime, and thus, particle motion was toward the nodes (see also Xie [32]).

Fig. 17 depicts a comparison between ripple celerity in our experiments and in Landry's experiments [36] for low ($R \approx 0.2$) and high reflective structures ($R \approx 0.9$). Ripple celerity is non-dimensional
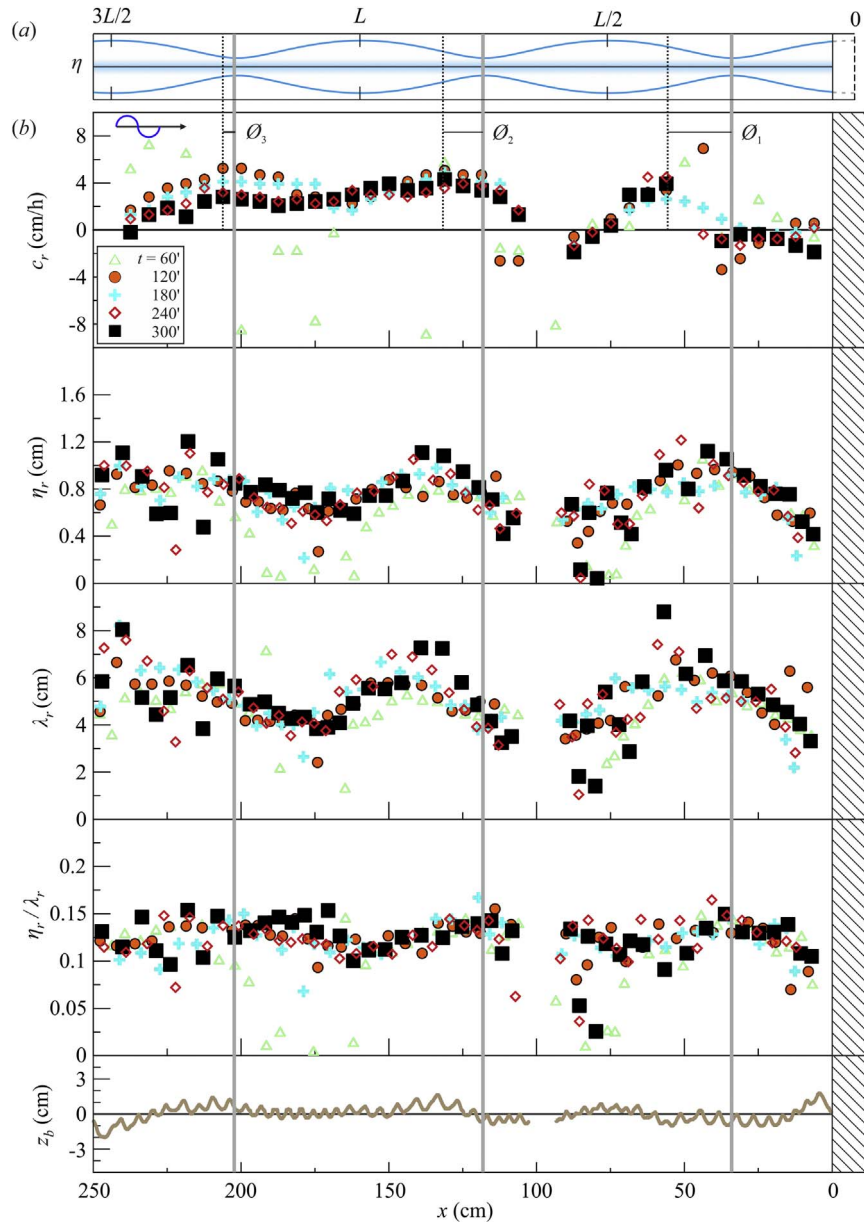
Fig. 14. Main characteristics of the ripples for Test 007 (random waves). (a) Wave envelope; (b) celerity, height, length, and steepness of the ripples at different times during the experiment. The last plot represents the bed profile at $t = 300$ min. Data are missing at $x \approx 95 - 100$ cm because of the presence of a vertical strut of the channel frame.

with respect to its maximum value on a $L/2$-length. As a reference, the free surface envelope and Lagrangian velocity inside the bottom boundary layer (at $\xi = 0.1$) are also given in the top panel (a) and middle panel (b), respectively. The absence of reflection ($R=0$) is equivalent to a constant uniform value of c_r (dotted horizontal line), while for increasing reflection, a space modulation of the celerity can be observed (dashed curve, fitting Landry's data), up to a linear trend for case $R \approx 0.9$ (continuous slanted line, fitting Landry's data).

The data from our experiments show a complex pattern which is locally influenced by the presence of the breakwater, and which depends on the phase shift of the reflected component. In the first half-wavelength (near the porous wall, $x \in [0\ L/2]$), a sequence of positive and negative values is observed, and Landry's curve represents a limiting positive envelope of our experimental results. The second half-wavelength ($x \in [L/2\ L]$) follows the sequence of Landry's experiments with negative celerity in the antinode and positive celerity elsewhere. Landry's interpolating curve for $R \approx 0.2$ has a maximum shifted to the lee side of the node envelope, with a generally positive celerity and a slightly negative celerity near the antinode.

Our data show a varying behavior near the breakwater, with negative celerity near the first quasi-node for certain experimental conditions, namely, large values of negative celerity near the first quasi-antinode (half the maximum positive celerity). Maximum celerities are almost near the quasi-nodes, without the shift of Landry's curve. In general, the present experimental data do not show a ripple celerity value between the empirical curves of Landry's experiments, but rather are controlled by local phenomena such as the scouring near the breakwater.

In our experiments the expected sediment transport was in bedload regime, since the Rouse number calculated from the maximum shear velocity was greater than $2 - 2.5$ (see Table 1). Following the procedure in Yu and Mei [51], we found an eddy viscosity on the order of $1.3\ \mathrm{cm^2 s^{-1}}$ and a thickness of the BBL of ≈ 0.7 cm, with a ratio $d_{50}/\delta \approx 0.05$. That means that the grains were in region $0 < \xi < 0.1$ where the Lagrangian velocity follows the trend in Fig. 17b. As a caveat, it should not be forgotten that (i) the Lagrangian velocity distribution inside the BBL is very sensitive to the boundary conditions at the domain (see Ng [62]); (ii) the Lagrangian velocity is influenced by
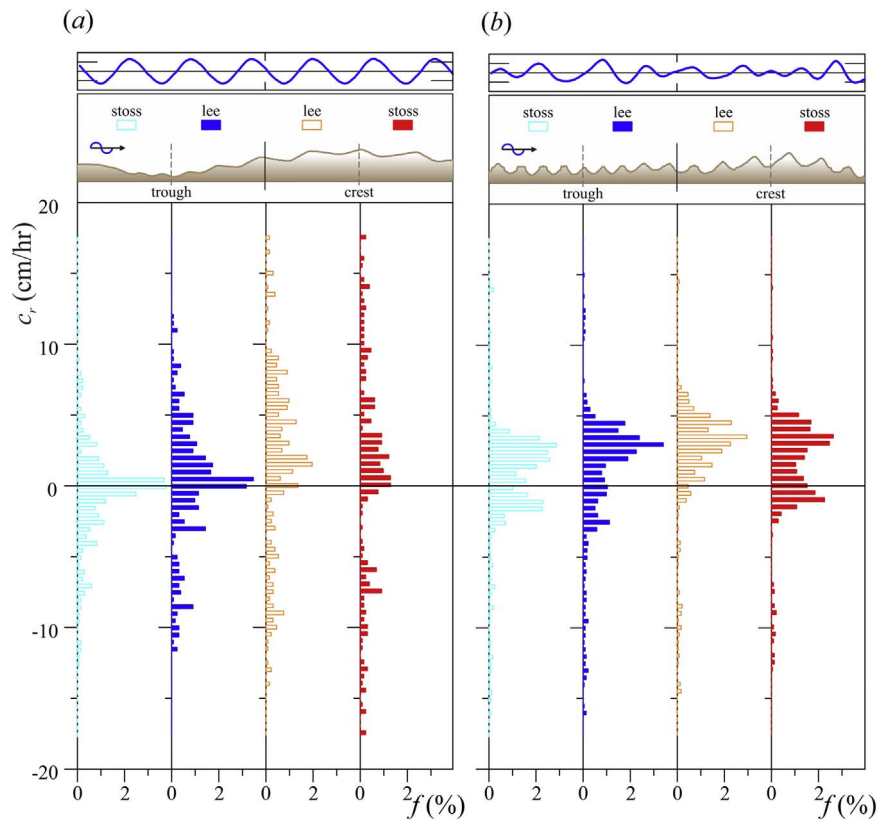
Fig. 15. Frequency distribution of ripple celerity. (a) Test006 (regular waves); (b) Test007 (random waves).
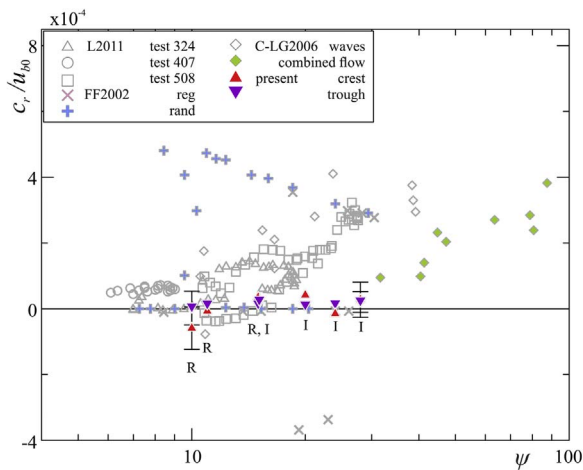

Fig. 16. Dimensionless ripple celerity. The symbols refer to the experiments by Faraci and Foti [22] (FF2002) for regular and random progressive waves; by Cataño-Lopera and García [59] (C-LG2006) for progressive waves only and waves plus current; by Landry [36] (L2011) for three tests in low-reflection and bedload-dominated conditions, with $R \approx 0.2$. Filled triangles indicate the ripple celerity in the crest and trough for our experiments, "R" and "I" stand for regular and irregular waves, respectively. The error bars are ± one standard deviation of the sample.

small currents associated with different process such as filtration through a porous breakwater; (iii) the structure of the BBL is significantly influenced by sandbars and streaming.

3.3.2. Ripple growth rate and celerity variations

In the present experiments in most cases (Test 001–007) the run started from a flat bed, in the other cases (Test 008–010) the new run started with the bottom left from the previous configuration.

Ripple growth is a process that is extremely dependent on flow energy conditions (Nielsen [17]). Accordingly, numerous relations have

been proposed for the prediction of ripple height and wavelength at equilibrium. There has been a great deal of research focused on ripple morphology and the time variation of the main morphological variables (see Pedocchi and Garcia [64] for and extensive review of relevant work). Doucette and O'Donoghue [24] introduced the concept of *dynamic equilibrium* and highlighted that while equilibrium conditions for all the variables (length, height, and celerity) do not depend on the initial conditions (i.e. flat bed or rippled bed), for a given forcing wave, the time required to reach equilibrium depends on the initial conditions. They expressed the time evolution of ripples height by means of a negative exponential form

$$\frac{\eta_r(t)}{\eta_e} = 1 - \left(1 - \frac{\eta_0}{\eta_e}\right)\exp\left[-\beta\frac{(t - t_0)}{T}\right],$$
(11)

where η_0 is the ripple height at the time t_0; η_e is the equilibrium height; and β is a coefficient representing the relaxation attitude of the system: large values of β indicate a fast approach to the asymptotic regime. Typical values are $\beta \approx O(10^{-3})$. Note that Eq. (11) has a structure that satisfies the compatibility conditions specified in Castillo et al. [65], namely, their Eq. (9).

Since equilibrium is a dynamic process, some fluctuations are expected even for long time series with a constant wave field. The time required to reach the equilibrium height of the ripple, $T_e = N_e T$ (where N_e is the number of wave cycles needed to reach the equilibrium) is defined as the time that it takes for the ripple height to be within 5% of the equilibrium ripple height η_e and to remain within 5% of η_e for several flow cycles (Smith and Sleath [23]; Doucette and O'Donoghue [24]). This definition can be better expressed in terms of the grain diameter, which is also the scale of the skin friction. It can thus be assumed that the equilibrium height of the ripples is the value that is either not exceeded or reached by a multiple of the grain diameter.

The concept of the equilibrium shape of ripples has been widely discussed in Losada et al. [9], who argued that the equilibrium state, defined by a constant energy dissipation rate, can be achieved by means
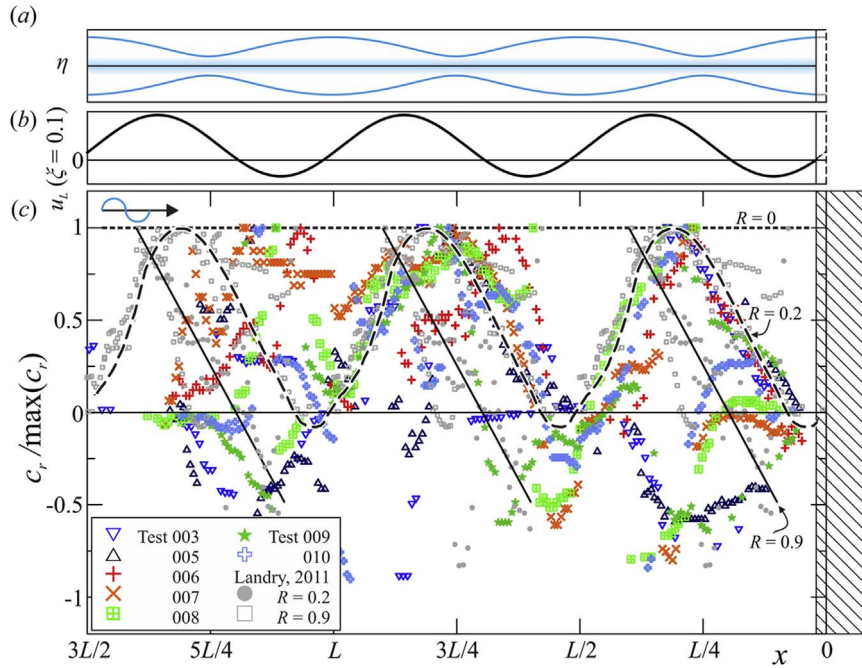
Fig. 17. Ripple celerity space distribution. (a) The free surface envelope, which differs slightly for different tests since the reflection coefficient varies; (b) Lagrangian velocity inside the bottom boundary layer at $\xi \equiv z/\delta = 0.1$ also slightly different for different tests; (c) our experiments in the asymptotic regime (symbols). Landry's experiments [36] (gray-filled circles and open squares). The horizontal dotted line refers to ripple celerity under progressive waves ($R=0$); the dashed curve interpolates Landry's data for the low reflecting case ($R \approx 0.2$); the straight continuous line interpolates Landry's data for the high reflective case ($R \approx 0.9$).
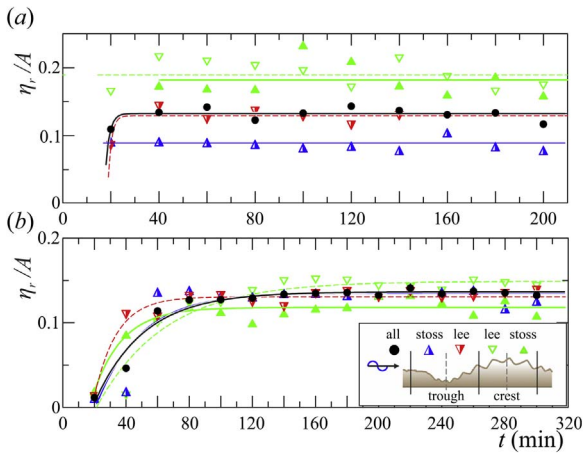

Fig. 18. Evolution of ripple median height. (a) Test 006 (regular waves); (b) Test 007 (random waves). The curves are the interpolating functions for ripples in the trough-stoss (blue), trough-lee (dashed red), crest-lee (dashed green), and crest-stoss (bold green). The black bold curve refers to all data. (For interpretation of the references to color in this figure legend, the reader is referred to the web version of this article).

Table 5
Parameters of ripple height growth for Test 006 and Test 007, regular and random waves, respectively.

		η_e/A	β ($\times 10^{-4}$)	N_e	v_η (cm/h)
		Test 006			
Crest	stoss	0.186	–	–	–
	lee	0.192	15.4	1700	4.77
Trough	stoss	0.091	–	–	–
	lee	0.129	156	200	32.4
Crest		0.189	139	200	42.4
Trough		0.101	3.4	6200	0.55
All		0.132	125	200	26.6
		Test 007			
Crest	stoss	0.118	11.6	3300	2.16
	lee	0.149	5.0	6900	1.17
Trough	stoss	0.135	7.7	4800	1.64
	lee	0.131	15.1	2800	3.12
Crest		0.141	5.7	6000	1.27
Trough		0.135	8.2	4500	1.74
All		0.137	7.0	5100	1.51

of different combinations of ripple height and wavelength. The system moves back and forth between various conditions, though within a limiting cycle, and moves away toward another limiting cycle only if the dissipation rate must change because of externally modified conditions. Losada et al. [9] introduced a coefficient $\epsilon = f_e/(d/A)^{3/4}$, where f_e is the energy dissipation factor, also related to the Nikuradse roughness height k_s as $k_s = 3.40\epsilon^{3/4}d$. For a given energy input (until the ripple disappears) there is an average shape of the ripples (height and wavelength) and the oscillations within the limiting cycle involves a specific number of grains. Near the upper limit of the existence of ripples, this number is quite large (ϵ almost 23), whereas near their initiation, the number of grains is rather low ($\epsilon \approx 1$).

Eq. (11) was obtained as a special case of the more general evolution differential equation [66]

$$\frac{d\eta}{dt} = \frac{\beta}{T}(\eta_e - \eta), \tag{12}$$

where T is the time scale of the process. The assumption is that all the parameters on the right side are time independent.

At the beginning of wave action, the growth rate is influenced by several factors, which also depend on the flume characteristics. For a closed system, ripple development is influenced by the equilibrium flows, which develops to satisfy the boundary conditions, as described in Ng [62]. Essentially, the growth rate β is not constant but rather varies over time. Although Eq. (11) has been proved to be generally correct, it does not suitably model initial transition. In order to better evaluate the parameters of ripple growth, we used the modified evolution equation:
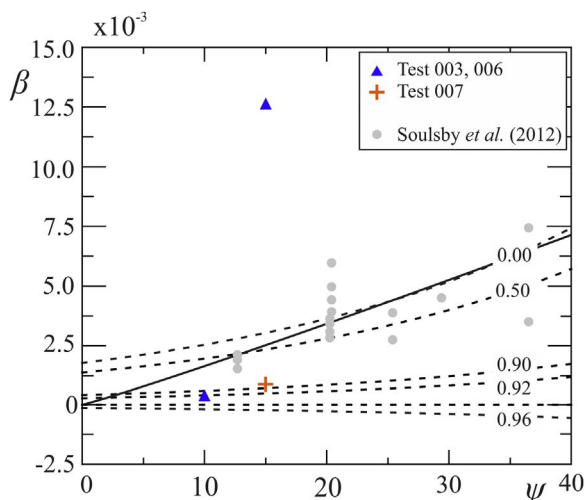
Fig. 19. Experimental and theoretical values of β. Solid line refers to Eq. (15) (Soulsby et al. [66]); dashed lines refer to Eq. (11) (Doucette and O'Donoghue [24]) for different values of the rate η_0/η_e.

$$\frac{\eta_r(t)}{\eta_e} = 1 - \left(1 - \frac{\eta_0}{\eta_e}\right)\exp\left[-\beta\frac{(t - t_s)}{T}\right], \tag{13}$$

which contains a shift time t_s that accounts for all of the neglected effects. In the present experiments t_s is of the order of a few minutes.

Fig. 18 shows the time evolution of ripple height for two tests with regular, and random waves, which where energetically equivalent and Table 5 lists the coefficients of Eq. (11) for these two tests. A column containing the average growth velocity has also been added, computed as $v_\eta = (\beta/T)(\eta_e - \eta_0)$. The analysis of the stratified sample indicated that the growth rate was different, depending on the position of the ripples in reference to the sandbars. The growth process was found to be faster for regular than for random waves.

Similar data can be evaluated for ripple wavelength and steepness,

Table 6
Median celerity of the ripples, based on their position in reference to the sandbars. Values are in cm/h, and data refer to the asymptotic regime. Positive values are in the direction of propagation of the incoming wave.

Test	ψ	Crest		Trough		Crest	Trough	All
		Stoss	Lee	Stoss	Lee			
005	10	−2.6	−5.3	0.7	−1.6	−4.9	0.2	−0.5
003	11	−1.3	4.9	−1.2	5.3	−0.6	0.9	0.4
006	15	3.1	4.3	1.1	1.1	3.6	1.1	2.8
007	15	0.8	3.0	1.3	2.4	2.5	2.3	2.4
008	20	2.7	5.3	0.8	3.4	4.9	0.9	2.3
009	24	−0.4	−2.0	1.5	1.5	−1.9	1.5	0.6
010	28	3.9	3.8	0.2	4.1	3.8	2.8	3.1

as shown in Appendix B in Figs. B.2–B.4 with the parameters in Tables B.2. For Test 007 (random waves), the initial steepness was smaller than the asymptotic equilibrium steepness, with ripple wavelength growing faster than the height. In contrast, the steepness was almost time-independent for Test 006 (regular waves) as though the ripple growth were homothetic, and the evolution equation were not a good model. Presumably there was a rapid growth of ripple steepness for Test 006, which is not evident because of the limited time resolution in the acquisition of the bed profiles.

Eq. (11) can be inverted to express the coefficient β as

$$\beta = 5.87 \times 10^{-4}\exp(0.036\psi)(\ln|1 - r_0| + 2.996), \tag{14}$$

where $r_0 = \eta_0/\eta_e$. Soulsby et al. [66] proposed the following estimate of the coefficient β for ripples generated only by progressive waves

$$\beta = \frac{2.996\psi^{1.07}}{21\,700 + \psi^{1.07}}, \tag{15}$$

This expression respects the asymptotic limit of a zero value for $\psi \to 0$. Fig. 19 shows the β values for the interpolating function as opposed to the mobility number. A comparison made to the data from three of our experiments and equations (Eqs. (14) and (15)). It was not possible to
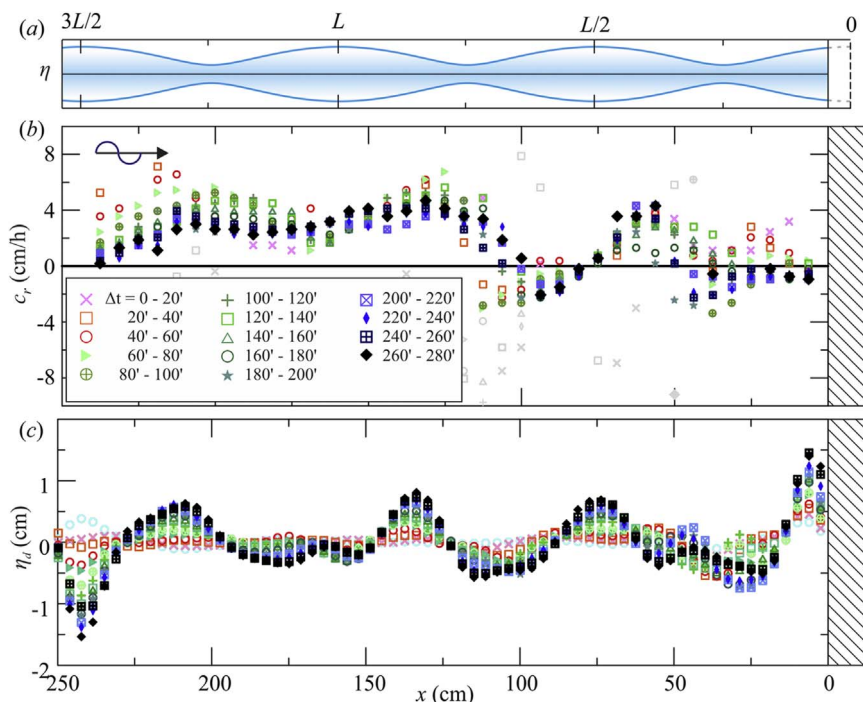

Fig. 20. Time evolution of ripples celerity for Test 007 (random waves). (a) Envelope of the free surface, computed with the phase shift of the reflected component $\Phi_2 = -0.527$ rad and a wavelength $L = 1.68$ m in reference to the peak period; (b) time stack of the ripple celerity for the 14 frame couples with a time interval of 20 min. The grey data are outliers caused by aliasing, vanishing, or appearance of new ripples; (c) time stack of the sandbars, same symbols and times used for (b).
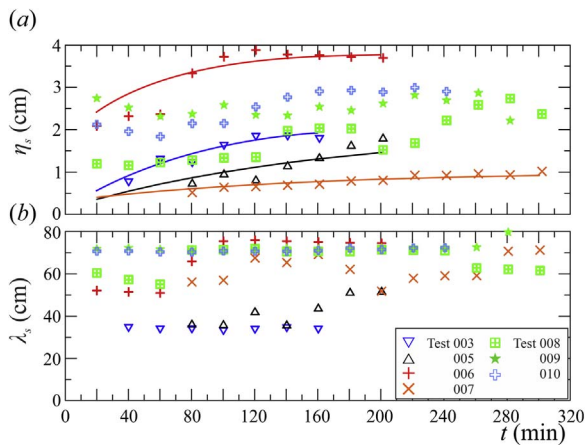
(a)

(b)

Fig. 21. Sandbar geometry evolution. (a) height; (b) wavelength of the sandbars.

elaborate the data for all our experiments since the time resolution of the video was not sufficiently high for a consistent estimation of the parameters of the evolution equation.

The difference between our experiments and the models in Soulsby et al. [66] and by Doucette and O'Donoghue [24] is evident. With specific reference to Test 006 and 007, the growth rate was much faster for regular than for random waves with the same mobility number value. Whereas the partially standing waves seemed to reduce growth rate values with respect to progressive random waves, the opposite was true for the regular partially standing waves, which favored fast-growing ripples that quickly reached the asymptotic regime when ripple height was considered.

Ripple celerity varies over time and space during the growth process of the bedforms and is controlled by various parameters that link sediments to flow-field characteristics. Fig. 20b shows the evolution of the migration celerity of ripples (c_r) for Test 007 (random waves) calculated by the correlation method in Section 2.3 under mildly reflective conditions. The surface envelope is plotted for reference in the top panel (Fig. 20a). As can be observed, a spatial modulation appears along the flume. The maximum c_r is located near the quasi-nodes while the minimum c_r is found next to the quasi-antinodes. Migration celerities range from -2 (opposite to the wave direction of propagation) to 6 cm/h (Table 6). In contrast, Faraci and Foti [22] observed a c_r under progressive waves of 7.2 cm/h ($\psi \approx 10$), Landry [36], in his experiments with wave-acting forces similar to those of our experiments, recorded a maximum c_r under low ($R \approx 0.2$) and high ($R \approx 0.9$) reflective conditions of 13 cm/h and 2.59 cm/h, respectively.

3.4. Sandbar morphology

Sandbar formation addresses to large-scale oscillations (Yalin [67]). As shown in Carter et al. [34], the reflection processes can be interpreted as a mechanism of sandbars generation. Mass transport induces recirculation cells in highly reflective beaches (Baquerizo et al. [53] and Yu and Mei [51], among others) and in front of breakwaters (Baquerizo and Losada [35], Baquerizo and Losada [50] and Gislason et al. [57], among others).

In our experiments, sandbars were quite evident and played a major role in the overall dynamics of ripples. This study provides little information on sandbar statistics and time evolution since there were only three or four sandbars at most, which is not a large sample. The sandbars suffered the end effects of the limited length of the sediment-covered flume. Furthermore, the duration of the experiments was not long enough to obtain the stationary state of sandbars morphology (if a stationary state can be ever reached). It should be also be remembered that sandbar geometry is controlled by the local water depth, which

becomes a key element in determining the maximum sandbar height and wavelength (Kennedy [68]).

In our experiments, the still water depth above the still sediment bed was equal to 20 cm, a very low value, which strongly influenced the sandbars. In light of these limits, Fig. 21 shows the sandbar height and wavelength. Sandbar height ranges from 1% to 2% of the free surface wavelength with a limited dispersion. An interpolating exponential curve was plotted only for tests starting from a flat bed. The horizontal asymptote was apparently not reached, even though for Test 007 (random waves), the time variations appeared to be quite limited during the last part of the experiment.

Sandbar wavelength can have different interpretations under regular and random waves (Fig. 21b). In our experiments, the ratio between the sandbar wavelength and ripple wavelength was $\overline{\lambda_s}/\overline{\lambda_r} \approx 10$. Regular waves creates a clear BAR region with sediments moving within. It was observed that sandbars that initially had a quarter of a wavelength subsequently evolved to $0.4L$. However, when the bed was attacked by random waves, the interaction between waves of several lengths led to the appearance of longer sandbars with a maximum wavelength of $L/2$, which is the length of the recirculation cells and the length found in the nature.

4. Discussion

The superposition of incoming and reflected waves creates spatial patterns where quasi-nodes and quasi-antinodes govern the modulation of the velocity and shear stress profiles at the bottom. This modulation favors ripple growth (if the critical bed shear is overcome) in the active region of the bed. The reflection modulus controls the generation of sandbars whereas the phase shift influences the location of ripples and sandbars.

Ripples in mid-reflecting conditions show a height, wavelength and steepness that are generally lower than those for ripples under progressive waves in the same energy conditions and with the same mobility number. There is a clear evidence of the modulating effect of the sandbars on ripples, with differences between the crest and trough regions of the sandbars.

Sandbar location and the free-surface envelope are directly connected since crests occur in the nodes, and troughs in the antinodes. However, there are some small shifts, and it seems that the crest-trough sequence in the sandbars of the sediment bottom is a more relevant controller for the ripples than the sequence of node-antinodes in the free-surface envelope. The ripples in the nodes of the free-surface envelope (sandbar crests) showed the best agreement with the classical formulas, while the ripples in the antinodes (sandbar troughs) had a size that was systematically over predicted. Differences were also found between the lee and stoss sides in sandbar crests and troughs. This was also evidence of two new process: roughness-induced streaming (Fuhrman et al. [69]) and bedform-induced shear stress (Hare et al. [70]).

The time scales of the two bedform families were well separated, and the duration of the experiments was sufficient for a complete development of the ripples but presumably not for a complete development of the sandbars. Sandbars also suffered the end effects of the length of the sediment bed. In addition, their size was constrained by the limited water depth. Under regular waves, the sandbar troughs were almost flat and without ripples. At most, they were subject to scouring.

Under random waves, the ripple population also spread in the sandbar troughs. The velocity of the ripple growth was studied by interpolating experimental data with empirical or semi-empirical models (Doucette and O'Donoghue [24], Soulsby et al. [66]). Our analysis clearly showed that ripples evolved faster under regular waves. The time evolution of the ripple steepness was not detected under regular waves. In all likelihood, this was due to the speed of the process, which caused the ripples to evolve without significant changes

in the steepness.

A significant contribution to the analysis of the ripples was the automatic detection of the celerity. The short-length cross-correlation algorithm gives different results, depending on the size of the window. If the window is larger than several wavelengths of the bedforms, the computed celerity can be excessively smoothed. We thus verified that the optimal size of the window was equal to 2–3 bedform wavelengths, with a satisfactory compromise between accuracy and resolution. In the presence of bedforms of substantially different lengths (e.g., sandbars plus ripples), the main components must also be separated by filtering them in the space domain or in the wavenumber domain. In the present tests, ripples and sandbars have been separated by filtering in the wavenumber domain the recorded bed profile (see also Landry [36]). The uncertainty in the estimated celerity is mainly due to the peak displacement detection since the measurement of the interval time Δt is extremely accurate. In addition to the uncertainty due to the camera resolution, optical distortion of the lenses, and the digitalization process of the bed profile, the cross-correlation algorithm has a minimum uncertainty of 1 pixel in the detection of the peak (less than 1 mm with the setup adopted). If the ripple experiences a displacement larger than a half-length in the two snapshots, an error occurs with a reverse sign of the detected velocity.

In general, the width of the window fixes the maximum wavenumber that can be detected without aliasing. In addition, the coalescence of ripples and growth of new ripples leads to an error since the algorithm is not able to elaborate the disappearance and appearance of new modulations of the bed profile. However, similar uncertainties are also encountered in the most commonly used manual methods and automatic detection algorithms of bedform peaks. Negative celerities of the ripples (opposite direction with respect to the incoming wave) are found near the vertical porous breakwater. Two main processes govern this fact. The first one involves the reverse directions of the horizontal Lagrangian velocity, which are permitted by the high local reflection coefficient (Carter et al. [34]; Landry [36]). The second is the return flow due to filtration through the porous breakwater (Losada et al. [49]). The mean current in the opposite direction of wave propagation created by the differences between the MWLs on the stoss and lee side of the breakwater, reduces the celerity observed along the flume. This effect can be seen as a linear reduction in space that creates another recirculation cell along the bed.

5. Conclusions

This paper has presented an innovative research study on ripple dynamics over a flat bed in a medium reflection environment, low incident energy conditions, bedload regime, and with non-breaking waves. It is an extension of the work on high and low reflective

conditions by Landry [36] and of the vast and diverse body of literature on ripples in the presence of progressive waves. The mid-reflection condition favors the spatial modulation of a bed with large-scale sandbars and small-scale ripples, and with some differences between regular and random waves. These spatial patterns are closely related to the position of quasi-nodes (or sandbar crests) where empirical formulas agree only with the largest ripples (at the sandbar crests). The ripples located in the antinodal regions and sandbar troughs showed a different pattern that requires further analysis.

The evolution of the large spatial scale (sandbars) influenced the small bedforms (ripples). Their size was found to be strongly constrained by the limited water depth (Nielsen and Shimamoto [71]). Since different values of the water depth could force different dynamics of the process, further study is needed.

The comparison between two equi-energetic wave conditions, with regular and random waves, clearly indicated that regular waves induced ripples that grew faster than those induced by random waves. This was evident in their height, wavelength and steepness.

In order to improve the analysis and to perform a more objective evaluation of bedform celerity, a method based on windowed cross-correlation (SLCC) of the digitized bed level was developed and successfully tested. The migration celerity of the ripples was also spatially modulated according to the crest-trough sequences, for both regular and random waves. The modulation of migration celerities was directly related to the Lagrangian velocity in the BBL (Landry [36]), with a trend closely linked to the Lagrangian velocity measured at $z/\delta = 0.1$, which was the scale of the sediment diameter. Finally, the phase shift of the reflection (as well as other mechanisms) was found to control ripple celerity, and to reverse the direction of the Lagrangian in the vicinity of the reflective element.

Appendix A. Measured fluid velocity

Fluid velocity was measured under stationary conditions in various sections of the flume (see Fig. 1). The instantaneous velocity modulated the shear stress near the bottom. However only when the threshold of sediment motion was overcome ($\theta_c \approx 0.05$), were ripples observed (Table 1). Fig. A.1 shows the measurements of the profiles of the phase-averaged $u-$ and $v-$ velocity components for a regular wave test. In the nodes, the horizontal velocity component u has a uniform profile, with values more than twice the values in the antinodes (Fig. A.1a and c) for the whole wave cycle. Maximum velocities of ≈ 30 cm s^{-1} were found, which were the same values expected from linear theory (see Table 1).

The vertical velocity component v had values approaching zero in the nodes (Fig. A.1b) and a linear increment in the z-axis near the antinodes (Fig. A.1d). A similar pattern was observed in other sections of the flume. The alternating pattern created by the reflection modified the $u-$ and $v-$ profiles with respect to a flat bottom. We assumed a velocity u_{b0} as represented by the maximum bottom velocity at each location for monochromatic waves and the mean velocity of the upper third for random waves (Doucette and O'Donoghue [24], Soulsby et al. [66]).

The choice of which waves are able to move the sediments in random waves is not unique, and in our analysis we chose the mean upper third for a straightforward comparison of the results with data obtained by other authors. The velocity amplitudes recorded in the experiments with random waves are shown in the Fig. A.2. The velocity profiles are similar to the regular wave profiles but less evident variations between nodal and antinodal sections were detected as a consequence of the somewhat unclear identification of nodes and antinodes for random waves.
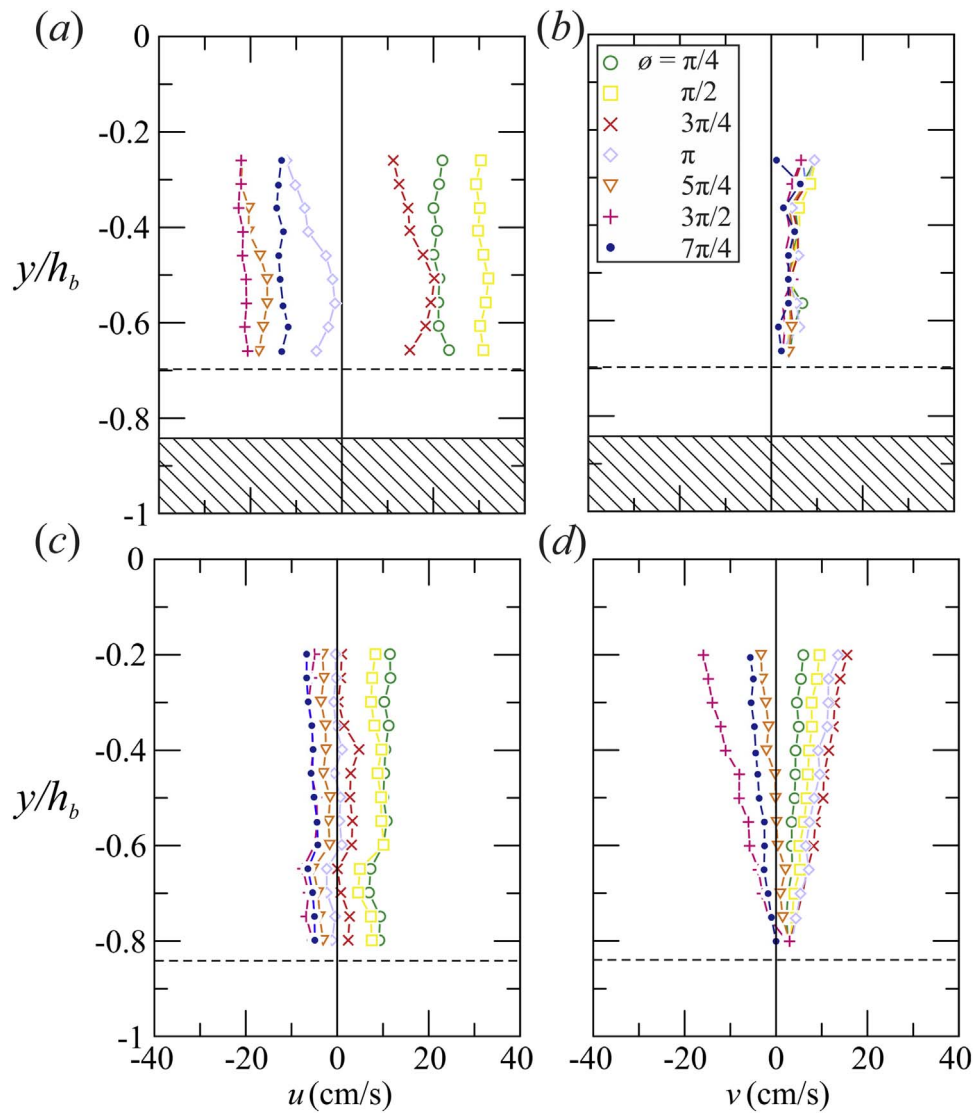
Fig. A.1. Horizontal and vertical phase-averaged velocity components for Test 006 (regular waves). (a) shows the horizontal velocity component; (b) shows the vertical velocity component in section #2, next to a nodal section; (c) and (d) show the velocity components in section #5, an antinodal section. The hatched area indicates the average local sediments bed. Below the dashed-line, no LDV measurements were obtained.
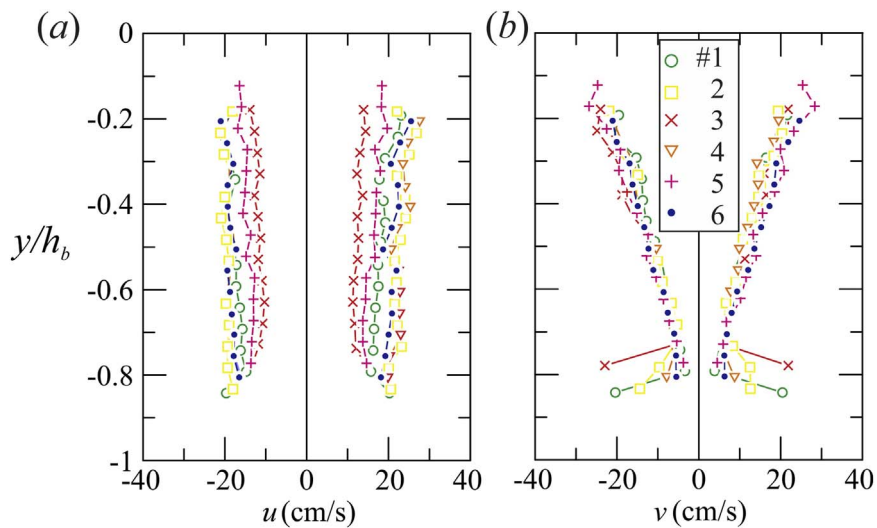

Fig. A.2. Velocity profiles measurements for Test 007 (irregular waves). (a) Horizontal velocity component; (b) vertical velocity component. The values refer to the average of the maximum one-third highest values in Sections #1–6 along the flume.

Appendix B. Wavelength and steepness evolution

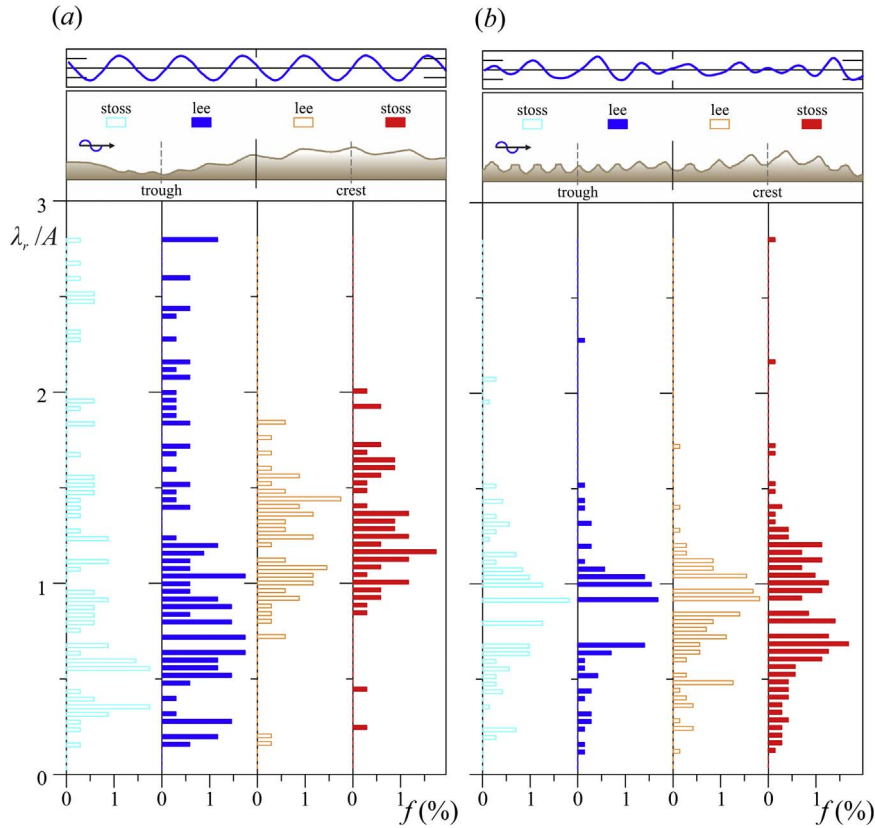See Figs. B.1–B.4 and Tables B.1-B.4.

Fig. B.1. Wavelength frequency of the ripples based on their position in reference to the sandbars. (a) Test 006 (regular waves); (b) Test 007 (random waves).
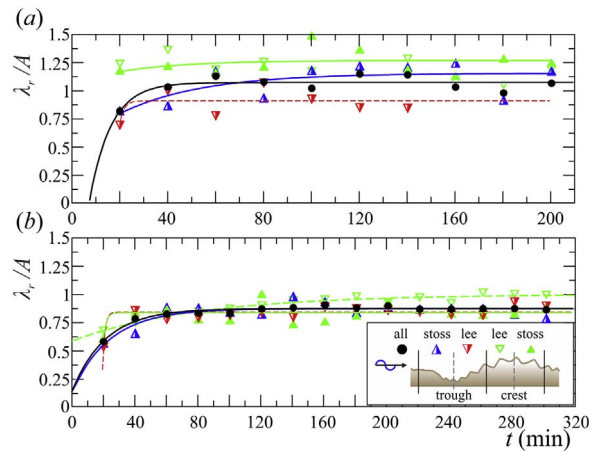

Fig. B.2. Evolution of ripple median wavelength. (a) Test 006 (regular waves); (b) Test 007 (random waves). The wavelength growth is not due to a variation of the forcing wave characteristics, but is attributed to a progressive adaptation of the bottom to the imposed wave regime.
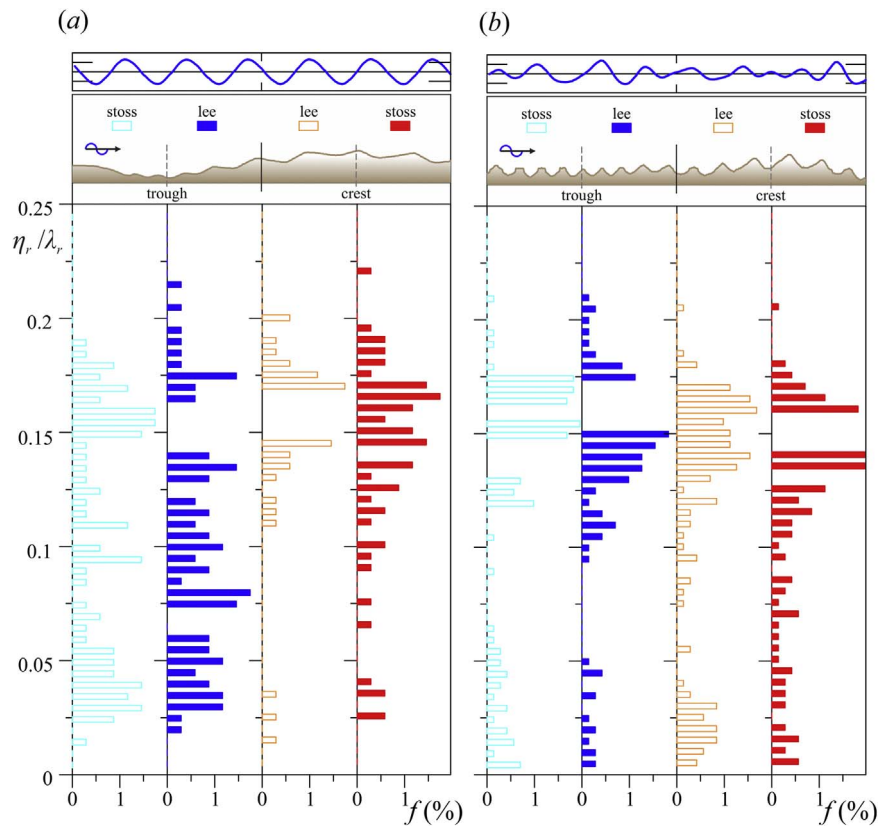
Fig. B.3. Frequency of the steepness of the ripples based on their position in reference to the sandbars. (a) Test 006 (regular waves); (b) Test 007 (random waves).
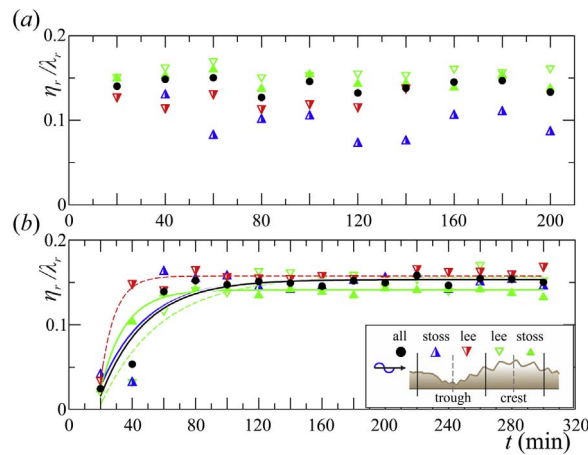

Fig. B.4. Evolution of ripple median steepness. (a) Test 006 (regular waves); (b) Test 007 (random waves).

Table B.1
Median wavelength of the ripples, based on their position in reference to the sandbars. The data refer to the asymptotic regime, and values are non-dimensional with respect to the wave orbital radius A.

Test	ψ	Crest		Trough		Crest	Trough	All
		Stoss	Lee	Stoss	Lee			
005	10	1.12	1.04	0.94	0.68	1.09	0.77	0.95
003	11	1.26	1.16	1.01	1.02	1.21	1.01	1.05
006	15	1.25	1.19	1.16	0.65	1.19	0.69	1.07
007	15	0.96	1.01	0.75	0.86	0.98	0.82	0.87
008	20	1.17	1.13	0.95	0.76	1.15	0.93	1.07
009	24	0.91	0.96	0.88	0.75	0.94	0.78	0.89
010	28	0.76	0.88	0.54	0.61	0.83	0.59	0.74

Table B.2
Parameters of ripple wavelength growth for Test 006 and Test 007, regular and random waves, respectively.

	Test 006			
	λ_e/A	β ($\times 10^{-4}$)	N_e	v_λ (cm/h)
Crest	stoss 1.270	7.8	3800	15.99
	lee –	–	–	–
Trough	stoss 1.155	6.4	4600	11.93
	lee 0.911	170	100	250.03
Crest	1.217	109	200	214.16
Trough	1.082	29	1000	50.66
All	1.075	24.2	1200	42.00
Test 007				
Crest	stoss 0.840	118	200	156.18
	lee 1.000	2.7	11000	4.25
Trough	stoss 0.875	9.1	3200	12.55
	lee 0.843	152	100	201.90
Crest	0.922	52	500	75.54
Trough	0.862	11.1	2600	15.08
All	0.875	10.1	2900	13.93

Table B.3
Median steepness of the ripples, based on their position in reference to the sandbars. The data refer to the asymptotic regime.

Test	θ	Crest		Trough		Crest	Trough	All
		Stoss	Lee	Stoss	Lee			
005	0.13	0.150	0.154	0.127	0.128	0.154	0.128	0.135
003	0.16	0.127	0.109	0.081	0.033	0.115	0.074	0.078
006	0.18	0.139	0.160	0.057	0.125	0.157	0.109	0.134
007	0.19	0.131	0.149	0.147	0.159	0.141	0.158	0.150
008	0.23	0.156	0.143	0.142	0.137	0.148	0.142	0.142
009	0.27	0.142	0.157	0.147	0.145	0.148	0.147	0.148
010	0.30	0.154	0.159	0.148	0.147	0.156	0.148	0.153

Table B.4
Parameters of ripple steepness growth for Test 006 and Test 007, regular and random waves, respectively.

	Test 006			
	$(\eta/\lambda)_e$	β	N_e ($\times 10^{-4}$)	$v_{\eta/\lambda}$ (h^{-1})
Crest	stoss 0.146	7.8	3800	0.32
	lee –	–	–	–
Trough	stoss 0.079	6.4	4600	0.14
	lee 0.142	170	100	6.67
Crest	0.155	109	200	4.69
Trough	0.093	29	1000	0.75
All	0.123	24.2	1200	0.82
Test 007				
Crest	stoss 0.141	14	2100	0.55
	lee 0.156	5.8	5100	0.25
Trough	stoss 0.154	7.5	3900	0.32
	lee 0.158	23.9	1200	1.05
Crest	0.148	7.6	3900	0.31
Trough	0.156	12.2	2400	0.53
All	0.153	7.6	3900	0.32

References

[1] A.R. Hunt, On the formation of ripplemark, Proc. R. Soc. Lond. 34 (220–223) (1882) 1–18 (1882).

[2] G.H. Darwin, On the formation of Ripple-Mark in Sand, Proc. R. Soc. Lond. 36 (228–231) (1883) 18–43 (1883).

[3] H. Ayrton, The origin and growth of ripple-mark, Proceedings of the Royal Society of London. Series A, Containing Papers of a Mathematical and Physical Character 84 (571) (1910) 285–310 (1910).

[4] R.A. Bagnold, G. Taylor, Motion of waves in shallow water. interaction between waves and sand bottoms, Proc. R. Soc. Lond. A: Math., Phys. Eng. Sci. 187 (1008) (1946) 1–18 (1946).

[5] R.A. Bagnold, An approach to the sediment transport problem from general physics, Geol. Surv. Prof. (1966) 1–37 (Paper 422-I).

[6] J.F.A. Sleath, Sea Bed Mechanics, Ocean Engineering, John Wiley & Sons, 1984.

[7] P.D. Komar, M.C. Miller, The threshold of sediment movement under oscillatory water waves, J. Sed. Pet. 43 (4) (1973) 1101–1110 (1973).

[8] M.A. Losada, J.M. Desiré, Incipient motion on a horizontal granular bed in non-breaking water waves, Coast. Eng. 9 (4) (1985) 357–370. http://dx.doi.org/10.1016/0378-3839(85)90017-1 (1985).

[9] M.A. Losada, J.M. Desiré, J. Merino, An energy approach to non-breaking wave-induced motion of bottom sediment particles, Coast. Eng. 11 (2) (1987) 159–173. http://dx.doi.org/10.1016/0378-3839(87)90005-6 (1987).

[10] P.L. Wiberg, C.K. Harris, Ripple geometry in wave-dominated environments, J. Geophys. Res.: Ocean. 99 (C1) (1994) 775–789. http://dx.doi.org/10.1029/93JC02726 (1994).

[11] J.F. Kennedy, The mechanics of dunes and antidunes in erodible-bed channels, J. Fluid Mech. 16 (1963) 521–544. http://dx.doi.org/10.1017/S0022112063000975 (1963).

[12] G. Vittori, P. Blondeaux, Sand ripples under sea waves part 2. finite-amplitude development, J. Fluid Mech. 218 (1990) 19–39. http://dx.doi.org/10.1017/S002211209000091X (9 1990).

[13] P. Nielsen, Coastal Bottom Boundary Layers and Sediment Transport, Advanced series on ocean Engineering, World Scientific, 1992.

[14] M. Manohar, Mechanics of bottom sediment movement due to wave action, Dayton: Armed Services Technical Information Agency, 1955.

[15] G. Mogridge, J. Kamphuis, Experiments on bed form generation by wave action, Proceedings, Coast. Eng. 1972 (1972) 1123–1142. http://dx.doi.org/10.1061/9780872620490.063 (1972).

[16] J. Dingler, D. Inman, Wave-formed ripples in nearshore sands, Proc. Coast. Eng. 1976 II (1976) 2109–2126 (1976).

[17] P. Nielsen, Dynamics and geometry of wave-generated ripples, J. Geophys. Res.: Ocean. 86 (C7) (1981) 6467–6472. http://dx.doi.org/10.1029/JC086iC07p06467.

[18] J.R. Allen, Sedimentary Structures Their Character and Physical Basis Volume I, Vol. 30, Part A of Developments in Sedimentology, Elsevier, 1982.

[19] D.L. Inman, Wave-generated ripples in nearshore sands, Beach Erosion Board, Tech. Memo 100, U. S. Army Corps of Engineers, 1957.

[20] J. R. Dingler, Wave formed ripples in nearshore sands, (Ph.D. thesis).

[21] P. Nielsen, 1DV structure of turbulent wave boundary layers, Coast. Eng. 112 (2016) 1–8 (2016).

[22] C. Faraci, E. Foti, Geometry, migration and evolution of small-scale bedforms generated by regular and irregular waves, Coast. Eng. 47 (1) (2002) 35–52. http://dx.doi.org/10.1016/S0378-3839(02)00097-2 (2002).

[23] D. Smith, J.F. Sleath, Transient ripples in oscillatory flows, Cont. Shelf Res. 25 (4) (2005) 485–501. http://dx.doi.org/10.1016/j.csr.2004.10.012 (2005).

[24] J.S. Doucette, T. O'Donoghue, Response of sand ripples to change in oscillatory flow, Sedimentology 53 (3) (2006) 581–596. http://dx.doi.org/10.1111/j.1365-3091.2006.00774.x (2006).

[25] Y.S. Chang, D.M. Hanes, Suspended sediment and hydrodynamics above mildly sloped long wave ripples, J. Geophys. Res.: Ocean. 109 (C7) (2004).

[26] J. Damgaard, R. Soulsby, A. Peet, S. Wright, Sand transport on steeply sloping plane and rippled beds, J. Hydraul. Eng. 129 (9) (2003) 706–719.

[27] R.C. Messaros, M.S. Bruno, Laboratory investigation of bedform geometry under regular and irregular surface gravity waves, J. Coast. Res. (2011) 94–103. http://dx.doi.org/10.2112/JCOASTRES-D-09-00062.1 (2011).

[28] J.S. Doucette, T. O'Donoghue, Sand ripples in irregular and changing wave conditions: A review of laboratory and field studies, Tech. rep., University of Aberdeen, Department of Engineering, Report for EC MAST Project No. MAS3-CT97-0086 Sandpit project (2002).

[29] P. Traykovski, A.E. Hay, J.D. Irish, J.F. Lynch, Geometry, migration, and evolution of wave orbital ripples at leo-15, J. Geophys. Res.: Ocean. 104 (C1) (1999) 1505–1524. http://dx.doi.org/10.1029/1998JC900026 (1999).

[30] P. Traykovski, Observations of wave orbital scale ripples and a nonequilibrium time-dependent model, J. Geophys. Res.: Ocean. 112 (C6) (2007) c06026. http://dx.doi.org/10.1029/2006JC003811.

[31] J.M. Turowski, Probability distributions for bed form-dominated bed load transport: the Hamamori distribution revisited, J. Geophys. Res.: Earth Surf. 116 (F2) (2011).

[32] S.-L. Xie, Scouring patterns in front of vertical breakwaters and their influences on the stability of the foundations of the breakwaters, Delft University of Technology, 1981.

[33] I. Irie, K. Nadaoka, Laboratory reproduction of seabed scour in front of break-waters, Coast. Eng. 1984 (1985) 1715–1731 (1985).

[34] T.G. Carter, P.L. Liu, C.C. Mei, Mass-transport by waves and offshore sand bedforms, J. Waterw. Harb. Coast. Eng. Div.-ASCE 99 (WW2) (1973) 165–184 (1973).

[35] A. Baquerizo, M.A. Losada, Longitudinal current induced by oblique waves along coastal structures, Coast. Eng. 35 (3) (1998) 211–230 (1998).

[36] B.J. Landry, Sand bed morphodynamics under water waves and vegetated conditions, (Ph.D. thesis), University of Illinois at Urbana-Champaign (2011).

[37] S. Longo, Wind-generated water waves in a wind tunnel: free surface statistics, wind friction and mean air flow properties, Coast. Eng. 61 (1) (2012) 27–41. http://dx.doi.org/10.1016/j.coastaleng.2011.11.008 (2012).

[38] I. Losada, R. Silva, M. Losada, Effects of reflective vertical structures permeability on random wave kinematics, J. Waterw., Port., Coast., Ocean Eng. 123 (6) (1997)

[39] C.L. Ting, W. Chao, C.-C. Young, Experimental investigation of nonlinear regular wave transformation over a submerged step: harmonic generation and wave height modulation, Coast. Eng. 117 (2016) 19–31 (2016).

[40] S. Baglio, C. Faraci, E. Foti, Structured light approach for measuring sea ripple characteristics, in: OCEANS '98 Conference Proceedings, , vol. 1, 1998, vol. 1 (Sep 1998) pp. 449–453 http://dx.doi.org/10.1109/OCEANS.1998.725787.

[41] H. Steinhaus, Sur la division des corp materiels en parties, Bull. Acad. Pol. Sci. 1 (1956) 801–804 (1956).

[42] A.M. Crawford, A.E. Hay, Linear transition ripple migration and wave orbital velocity skewness: observations, J. Geophys. Res.: Ocean. 106 (C7) (2001) 14113–14128. http://dx.doi.org/10.1029/2000JC000612 (2001).

[43] P. Hoekstra, P. Bell, P. van Santen, N. Roode, F. Levoy, R. Whitehouse, Bedform migration and bedload transport on an intertidal shoal, Cont. Shelf Res. 24 (11) (2004) 1249–1269 (2004).

[44] S. Yalin, R. Russell, Similarity in sediment transport due to waves, Proc. Coast. Eng. 1962 (1962) 151–167 (1962).

[45] J.F.A. Sleath, On rolling-grain ripples, J. Hydraul. Res. 14 (1) (1976) 69–81. http://dx.doi.org/10.1080/00221687609499689 (1976).

[46] A.M. Crawford, Field observations of linear transition ripple migration and wave orbital velocity skewness, (Ph.D. thesis), University of Newfoundland (2000).

[47] T. O'Donoghue, J.S. Doucette, J.J. van der Werf, J.S. Ribberink, The dimensions of sand ripples in full-scale oscillatory flows, Coast. Eng. 53 (12) (2006) 997–1012. http://dx.doi.org/10.1016/j.coastaleng.2006.06.008 (2006).

[48] I.G. Jonsson, Wave boundary layers and friction factors, Proc. Coast. Eng. 1 (10) (1966) (1996).

[49] I.J. Losada, R.A. Dalrymple, M.A. Losada, Wave-induced mean flows in vertical rubble mound structures, Coast. Eng. 35 (4) (1998) 251–281 (1998).

[50] A. Baquerizo, M.A. Losada, Sediment transport around a mound breakwater: the toe erosion problem, Coast. Eng. Proc. 1 (1998) 26 (1998).

[51] J. Yu, C.C. Mei, Formation of sand bars under surface waves, J. Fluid Mech. 416 (2000) 315–348 (2000).

[52] A. Baquerizo, Wave reflection on beaches: Methods of assessment and. forecasting, (Ph.D. thesis), University of Cantabria (in Spanish) (1995).

[53] A. Baquerizo, M. Losada, J. Smith, N. Kobayashi, Cross-shore variation of wave reflection from beaches, J. Waterw., Port., Coast., Ocean Eng. 123 (5) (1997) 274–279. http://dx.doi.org/10.1061/(ASCE)0733-950X(1997)123:5(274) (1997).

[54] S.A. Hughes, J.E. Fowler, Estimating wave-induced kinematics at sloping structures, J. Waterw., Port., Coast., Ocean Eng. 121 (4) (1995) 209–215. http://dx.doi.org/10.1061/(ASCE)0733-950X(1995)121:4(209) (1995).

[55] J. Sutherland, T. O'Donoghue, Wave phase shift at coastal structures, J. Waterw., Port., Coast., Ocean Eng. 124 (2) (1998) 90–98 (1998).

[56] B.M. Sumer, J. Fredsøe, Experimental study of 2D scour and its protection at a rubble-mound breakwater, Coast. Eng. 40 (1) (2000) 59–87 (2000).

[57] K. Gíslason, J. Fredsøe, R. Deigaard, B.M. Sumer, Flow under standing waves: part 1. shear stress distribution, energy flux and steady streaming, Coast. Eng. 56 (3) (2009) 341–362. http://dx.doi.org/10.1016/j.coastaleng.2008.11.001 (2009).

[58] M. Carstens, F. Nielson, H. Altinbilek, Bed forms generated in the laboratory under oscillatory flow, Tech. rep., Coastal Eng. Res. Cent., Fort Belvoir, Va (1969).

[59] Y.A. Cataño-Lopera, M.H. García, Geometry and migration characteristics of bedforms under waves and currents: part 2: ripples superimposed on sandwaves, Coast. Eng. 53 (9) (2006) 781–792 (2006).

[60] J.F.A. Sleath, A contribution to the study of vortex ripples, J. Hydraul. Res. 13 (3) (1975) 315–328 (1975).

[61] K. Horikawa, A. Watanabe, A study on sand movement due to wave action, Coast. Eng. Jpn. 10 (1967) 39–57 (1967).

[62] C. Ng, Mass transport in gravity waves revisited, J. Geophys. Res.: Ocean. 109 (C4) (2004).

[63] B.J. Landry, M.J. Hancock, C.C. Mei, Note on sediment sorting in a sandy bed under standing water waves, Coast. Eng. 54 (9) (2007) 694–699 (2007).

[64] F. Pedocchi, M.H. García, Ripple morphology under oscillatory flow: 1.prediction, J. Geophys. Res.: Ocean. 114 (C12) (2009).

[65] C. Castillo, E. Castillo, A. Fernández-Canteli, R. Molina, R. Gómez, Stochastic model for damage accumulation in rubble-mound breakwaters based on compatibility conditions and the central limit theorem, J. Waterw., Port., Coast., Ocean Eng. 138 (6) (2012) 451–463 (2012).

[66] R.L. Soulsby, R.J.S. Whitehouse, K.V. Marten, Prediction of time-evolving sand ripples in shelf seas, Cont. Shelf Res. 38 (2012) 47–62. http://dx.doi.org/10.1016/j.csr.2012.02.016 (2012).

[67] S. Yalin, Mechanics of Sediment Transport, Pergamon, 1972.

[68] J.F. Kennedy, The formation of sediment ripples, dunes, and antidunes, Annu. Rev. Fluid Mech. 1 (1) (1969) 147–168. http://dx.doi.org/10.1146/annurev.fl.01.010169.001051 (1969).

[69] D.R. Fuhrman, B.M. Sumer, J. Fredsøe, Roughness-induced streaming in turbulent wave boundary layers, J. Geophys. Res.: Ocean. 116 (C10) (2011).

[70] J. Hare, A.E. Hay, L. Zedel, R. Cheel, Observations of the space-time structure of flow, turbulence, and stress over orbital-scale ripples, J. Geophys. Res.: Ocean. 119 (3) (2014) 1876–1898 (2014).

[71] P. Nielsen, T. Shimamoto, Bar response to tides under regular waves, Coast. Eng. 106 (2015) 1–3 (2015).